On Symmetric Instabilities in Oceanic Bottom Boundary Layers

J. S. ALLEN AND P. A. NEWBERGER

College of Oceanic and Atmospheric Sciences, Oregon State University, Corvallis, Oregon

(Manuscript received 21 February 1997, in final form 5 September 1997)

ABSTRACT

Model studies of two-dimensional, time-dependent, wind-forced, stratified downwelling circulation on the continental shelf have shown that the near-bottom offshore flow can develop time- and space-dependent fluctuations involving spatially periodic separation and reattachment of the bottom boundary layer and accompanying recirculation cells. Based primarily on the observation that the potential vorticity Π, initially less than zero everywhere, is positive in the region of the fluctuations, this behavior was identified as finite amplitude slantwise convection resulting from a symmetric instability. To further support that identification, a direct stability analysis of the forced, time-dependent, downwelling circulation would be useful, but is difficult because the instabilities develop as an integral part of the evolving flow field. The objectives of the present study are 1) to examine the linear stability of a near-bottom oceanic flow over sloping topography with conditions dynamically similar to those in the downwelling circulation and 2) to establish a link between the instabilities observed in the wind-forced downwelling problem and the results of recent theoretical studies of bottom boundary layer behavior in stratified oceanic flows over sloping topography. These objectives are addressed by investigating the two-dimensional linear stability and the nonlinear behavior of the steady, inviscid, ''arrested Ekman layer'' solution produced by transient downwelling in one-dimensional models of stratified flow adjustment over a sloping bottom. A linear stability analysis shows that this solution is unstable to symmetric instabilities and confirms that a necessary condition for instability is $\Pi > 0$ in the bottom layer. Numerical experiments show that the unstable, time-dependent, nonlinear behavior in the boundary layer involves the formation of slantwise circulation cells with characteristics similar to those found in the wind-forced downwelling circulation and the development of weak stable stratifiction close to that corresponding to marginally stable conditions with $\Pi = 0$.

1. Introduction

The time-dependent response of a stratified coastal ocean initially at rest to constant downwelling-favorable alongshore wind stress was studied in Allen and Newberger (1996). The Blumberg–Mellor (1987), hydrostatic, primitive equation model was utilized for numerical experiments in an idealized two-dimensional situation that included spatial variations across-shelf and with depth, but assumed uniformity alongshore. Bottom topography typical of the continental shelf and slope from the Oregon coast was used. The results show new behavior of downwelling flow fields including the formation of downwelling fronts and the development of time- and space-dependent variability in the near-bottom offshore flow. Of interest here is the latter feature in which the across-shelf circulation near the bottom is characterized by time- and space-dependent fluctuations involving spatially periodic separation and reattachment of the bottom boundary layer and accompanying recirculation cells. Typical spatial scales of these fluctuations are 3–5 km in the horizontal and 20–70 m in the vertical. In addition, a general tendency for the fluctuations to propagate onshore at a rate of about 1–3 km/day is found.

The behavior of the near-bottom flow was identified in Allen and Newberger (1996) as finite amplitude slantwise convection resulting from a hydrostatic symmetric instability. That conclusion was based primarily on the fact that the potential vorticity Π, which was negative everywhere initially, became positive in the region of these fluctuations. Geostrophically balanced, steady flows in an unbounded region with stable stratification are unstable to two-dimensional inviscid perturbations if the potential vorticity $\Pi > 0$ (Ooyama 1966; Hoskins 1974; Bennetts and Hoskins 1979). [Note that the definition of Π in Allen and Newberger (1996) reverses the sign of the potential vorticity in the condition for instability compared to the sign in the above references.] These so-called symmetric instabilities involve a combination of the mechanisms responsible for inertial instability in a rotating unstratified flow and for convective instability in a stratified nonrotating flow (Emanuel 1994). A relevant point concerning the downwelling circulation is that symmetric instabilities can develop in rotating, stratified flow situations stable to both pure

Corresponding author address: Dr. John S. Allen, College of Oceanographic and Atmospheric Sciences, Oregon State University, 104 Ocean Admin. Bldg., Corvallis, OR 97331-5503.
E-mail: jallen@oce.orst.edu

inertial instability or pure convective instability. Thus, as the across-shelf flow under downwelling conditions attempts to push lower density fluid under higher density fluid, symmetric instabilities can develop before the flow becomes convectively unstable, that is, before the vertical density gradient becomes positive. Additional features of the time- and space-dependent fluctuations in the downwelling experiments in Allen and Newberger that support the identification of the behavior as due to finite amplitude symmetric instabilities [alternatively called slantwise convection, Emanuel (1994)] are the observations that the streamlines in the flow in the bottom layer are dominantly aligned slantwise along the direction of the density surfaces and that a major part of the process is governed by inviscid dynamics.

The necessary condition for symmetric instability of positive potential vorticity, appealed to in Allen and Newberger (1996), is readily derived for inviscid perturbations of an unbounded, steady, geostrophically balanced flow (e.g., Bennetts and Hoskins 1979). The analysis by Ooyama (1966), which establishes a sufficient condition for instability in a baroclinic circular vortex, helps support application of that condition locally. It would be desirable, nevertheless, to be able to appeal to a stability analysis directly applicable to the particular downwelling flow field of interest. Efforts to formulate a stability problem relevant to the steadily forced downwelling circulation are frustrated by the fact that the instabilities develop as an integral part of the time-dependent evolution of the total flow field. In other words, for that case a basic-state flow that satisfies the equations and is appropriate for a stability analysis is not readily identifiable.

The objectives of the present study are twofold. The first is to formulate and examine the stability of an idealized near-bottom flow with conditions dynamically similar to those in the downwelling circulation. The second is to establish a link between the symmetric instabilities observed in the wind-forced downwelling problem and the results of recent theoretical studies of bottom boundary layer behavior in stratified oceanic flows over sloping topography (Trowbridge and Lentz 1991; MacCready and Rhines 1993; Garrett et al. 1993). To accomplish these objectives we focus on a conceptually important result arrived at by both Trowbridge and Lentz (1991) and MacCready and Rhines (1993). In particular, in one-dimensional stratified flow problems, that is, with velocity variations only in the direction normal to the slope, they investigated the time-dependent adjustment of an initially uniform, geostrophically balanced alongshore velocity to the bottom boundary condition of no-slip. Cases where the resultant Ekman transport was either upslope (upwelling) or downslope (downwelling) were examined. In the downwelling case of interest here, it is found that the combination of downslope Ekman transport and density mixing processes result in a boundary layer, characterized by uniform well-mixed density normal to the surface, increasing in height with time. The boundary layer stops growing and the flow equilibrates when the height of the boundary layer is large enough that the geostrophically balanced vertical shear, associated through the thermal wind balance with the resulting alongslope gradients of density, can adjust the interior velocity to a zero value at the bottom boundary. This results in a ''shutdown'' of the frictionally related Ekman transport (MacCready and Rhines 1993). The equilibrated flow is in inviscid geostrophic balance and has been described as evolving from an ''arrested Ekman layer'' (Garrett et al. 1993). We note that a dynamically similar equilibrated flow occurs [as a result of modeling approximations similar to those in Trowbridge and Lentz (1991)] in a problem considered recently by Chapman and Lentz (1997) for the steady, spatially dependent adjustment of an alongslope current over sloping topography.

It seems that an investigation of the stability properties of the arrested Ekman layer equilibrium solution produced by transient downwelling would be highly desirable in any case, but especially so in light of the results from the wind-forced downwelling experiments in Allen and Newberger (1996). The arrested Ekman layer equilibrium flow is steady, inviscid, and geostrophically balanced and thus provides a reasonable basic state for a stability analysis. We pursue that stability analysis here.

An outline of the paper is as follows. The two-dimensional inviscid, linear stability problem for the arrested Ekman layer geostrophic equilibrium solution is formulated in section 2 and solved in section 3. (The linear stability of a related basic-state flow with a somewhat different structure is examined in appendix A and the alteration of the results of the linear stability analysis by the inclusion of weak dissipative effects is addressed in appendix B.) The resulting finite amplitude behavior is studied with numerical experiments in section 4. A summary of the conclusions is given in section 5. It will be shown that the equilibrium solution is unstable to symmetric instabilities. It will also be shown that at finite amplitude the near-bottom flow develops time- and space-dependent fluctuations involving the formation of slantwise circulation cells with streamlines aligned dominantly along density surfaces that are similar to the across-shelf circulation patterns found in the downwelling experiments in Allen and Newberger (1996).

2. Formulation

We consider rotating, stratified fluid motion on an f plane governed by the hydrostatic primitive equations. The equations in Cartesian coordinates (x, y, z) for inviscid, two-dimensional $(\partial/\partial y = 0)$ flow are

$$u_x + w_z = 0, \tag{2.1a}$$

$$\frac{Du}{Dt} - fv = -p_x/\rho_0, \tag{2.1b}$$

$$\frac{Dv}{Dt} + fu = 0, \tag{2.1c}$$

$$0 = -p_z - \rho g, \tag{2.1d}$$

$$\frac{D\rho}{Dt} = 0, \tag{2.1e}$$

where $\mathbf{x} = (x, y, z)$, the velocity $\mathbf{u} = (u, v, w)$,

$$\frac{D}{Dt} = \left(\frac{\partial}{\partial t} + \mathbf{u}\cdot\nabla\right), \tag{2.2}$$

and where p is the pressure, t is time, subscripts (x, y, z, t) denote partial differentiation, f is the constant Coriolis parameter, and g is the acceleration of gravity. The total density $\rho_T = \rho_0 + \rho$, where ρ_0 is a constant reference density. We assume $f > 0$.

The y-momentum equation (2.1c) implies the conservation of absolute momentum M on fluid particles,

$$\frac{DM}{Dt} = 0, \tag{2.3}$$

where

$$M = v + fx. \tag{2.4}$$

In addition, (2.1) imply the conservation of potential vorticity Π on fluid particles,

$$\frac{D\Pi}{Dt} = 0, \tag{2.5}$$

where

$$\Pi = (f + v_x)\rho_z - v_z\rho_x, \tag{2.6a}$$

$$= J(M, \rho), \tag{2.6b}$$

and where the operator $J(a, b) = a_x b_z - a_z b_x$ is the Jacobian.

The x-momentum equation (2.1b) may be written as

$$\frac{Du}{Dt} = f(M - M_g), \tag{2.7}$$

where

$$M_g = V + fx, \qquad V = -p_x/(f\rho_0). \tag{2.8a,b}$$

Equation (2.7) may be utilized, together with (2.3), as the basis for parcel displacement arguments to establish the condition $\partial M_g/\partial x < 0$ for inertial instability of the geostrophic flow V (Emanuel 1994; Holton 1992). When the flow is stratified and hydrostatic, with a geostrophic velocity V in thermal wind balance with a density field $\overline{\rho}$, flow perturbations will tend to align along the density surfaces. This suggests that, in the subsequent arguments for instability, we should consider evaluation of $\partial M_g/\partial x$ along $\overline{\rho}$ surfaces (Emanuel 1994, sections 12.1–12.3; Holton 1992, sections 7.5–9.3). As a consequence, the possible occurrence of unstable motions, termed symmetric instability or slantwise convection, depends on the relative orientation of the M_g and $\overline{\rho}$ surfaces. Relevant information concerning that orientation is provided by the sign of the potential vorticity $\Pi = J(M_g, \overline{\rho})$. Thus, if $\Pi > 0$ the flow is found to be unstable to parcel displacements along $\overline{\rho}$ surfaces (Emanuel 1994; Holton 1992). Again, we note that the definition of Π (2.6) reverses the sign of the potential vorticity in the condition for instability compared to the sign in most of the referenced papers where potential vorticity is defined utilizing potential temperature.

To examine the stability of the arrested Ekman layer equilibrium flow directly, we pursue a linear stability analysis. We consider small perturbations to a basic-state flow that comprises a steady, geostrophically balanced velocity $V(x, z)$ in the y direction in thermal wind balance with the density field $\overline{\rho}(x, z)$, so that

$$fV_z = -g\overline{\rho}_x/\rho_0. \tag{2.9}$$

Thus, we assume

$$v = V(x, z) + v', \qquad u = u', \qquad w = w', \tag{2.10a,b,c}$$

$$\rho_T = \rho_0 + \overline{\rho}(x, z) + \rho', \qquad p = P(x, z) + p', \tag{2.10d,e}$$

where the primed variables are small perturbations dependent on (x, z, t).

The resulting inviscid equations, with the primes on the perturbation variables omitted, are

$$u_x + w_z = 0 \tag{2.11a}$$

$$u_t - fv = -p_x/\rho_0, \tag{2.11b}$$

$$v_t + uV_x + wV_z + fu = 0, \tag{2.11c}$$

$$0 = -p_z - \rho g, \tag{2.11d}$$

$$\rho_t + u\overline{\rho}_x + w\overline{\rho}_z = 0. \tag{2.11e}$$

As a result of the two-dimensional approximation, a perturbation streamfunction ψ that satisfies (2.11a) may be defined where

$$u = \psi_z, \qquad w = -\psi_x. \tag{2.12a,b}$$

A single equation for ψ may be derived from (2.11) (e.g., Bennetts and Hoskins 1979) by taking the z and t derivations of (2.11b) to obtain

$$u_{ztt} = (fv_z + g\rho_x/\rho_0)_t \tag{2.13}$$

and then eliminating v_{zt} and ρ_{xt} using the z derivative of (2.11c) and the x derivative of (2.11e). The resulting equation for ψ is

$$\psi_{zztt} = -f(f + V_x)\psi_{zz} + (fV_z - g\overline{\rho}_x/\rho_0)\psi_{xz} - N^2\psi_{xx} - \psi_z I_x + \psi_x I_z, \quad (2.14)$$

where

$$I = fV_z + g\overline{\rho}_x/\rho_0 \quad (2.15a)$$

and

$$N^2(x, z) = -g\overline{\rho}_z/\rho_0. \quad (2.15b)$$

As a consequence of (2.9), $I = 0$ and (2.14) reduces, without restriction on the (x, z) variability of the basic-state flow, to

$$\psi_{zztt} = -f(f + V_x)\psi_{zz} + 2fV_z\psi_{xz} - N^2\psi_{xx}. \quad (2.16)$$

We note from the right-hand side of (2.13) that, although the basic state is geostrophically balanced (2.9), it is the departure from geostrophic balance in the perturbation field that drives the time variability of u_z (Bennetts and Hoskins 1979).

We consider the fluid motion in a semi-infinite region above a uniformly sloping bottom. The bottom surface is a plane at an angle α from the horizontal with z coordinate given by

$$z = x\tan\alpha. \quad (2.17)$$

We utilize a coordinate system (x', z') formed by rotating the axes so that z' is perpendicular to the bottom. The transformation of coordinates is given by

$$x' = x\cos\alpha + z\sin\alpha, \qquad z' = -x\sin\alpha + z\cos\alpha. \quad (2.18)$$

We also define dimensionless independent variables

$$\xi = x'\tan\alpha/\delta, \qquad \zeta = z'/\delta, \qquad \hat{t} = tf, \quad (2.19a,b,c)$$

where δ is a length scale, defined below, corresponding to the height of the initial inviscid boundary layer.

We assume that

$$\tan^2\alpha \ll 1, \quad (2.20)$$

and that the slope Burger number

$$S(x, z) = (N^2/f^2)\tan^2\alpha = O(1). \quad (2.21)$$

After transforming (2.16) to coordinates (2.18), rewriting in terms of the dimensionless variables in (2.19), and neglecting small terms $O(\tan^2\alpha)$ we obtain

$$\psi_{\zeta\zeta\hat{t}\hat{t}} = -\{[1 + (V_x/f)] + 2(V_z/f)\tan\alpha + S\}\psi_{\zeta\zeta} + 2[(V_z/f)\tan\alpha + S]\psi_{\xi\zeta} - S\psi_{\xi\xi}, \quad (2.22)$$

where, as shown below,

$$(V_z/f)\tan\alpha = O(1), \qquad (V_x/f) = O(1). \quad (2.23a,b)$$

We assume that, outside of a boundary layer of height δ, the basic-state flow is a uniform, depth-independent velocity V_0 with uniform stratification of constant $N^2 = N_0^2$. In the boundary layer we assume that the geostrophic basic-state flow varies only with ζ. Specifically, we assume that

$$V = V(\zeta) = V_0 + V'(\zeta) \quad (2.24a)$$

and

$$N^2 = N^2(\zeta) = -g\overline{\rho}_z/\rho_0 = N_0^2 + N'^2(\zeta), \quad (2.24b)$$

where V_0 and N_0^2 are constants,

$$V(0) = V_0 + V'(0) = 0, \quad (2.25)$$

$$V'(\zeta) \to 0, \qquad N'^2(\zeta) \to 0 \quad \text{for } \zeta \gg 1. \quad (2.26a,b)$$

We assume that the basic-state flow is stably (or neutrally) stratified,

$$N^2 = N_0^2 + N'^2(\zeta) \geq 0. \quad (2.27)$$

The boundary layer variations $V'(\zeta)$ and $N'^2(\zeta)$ are specified by the geostrophic pressure function,

$$p_0'(\zeta) = -\delta\rho_0 f V_0 R(\zeta)/\sin\alpha, \quad (2.28)$$

where $R(\zeta)$ is dimensionless. The scaling for the pressure $p_0'(\zeta)$ in (2.28) is chosen so that $V' = p_{0x}'/(\rho_0 f) = V_0 R_\zeta$. In addition, to allow for situations where the stratification in the boundary layer may take on different magnitudes, we define a dimensionless parameter γ so that $N'^2 = p_{0zz}'/\rho_0 = -\gamma N_0^2 R_{\zeta\zeta}$,

$$\gamma = fV_0\cos^2\alpha(\delta N_0^2\sin\alpha)^{-1} = V_0\sin\alpha(\delta f S_0)^{-1}, \quad (2.29)$$

$$S_0 = (N_0^2/f^2)\tan^2\alpha. \quad (2.30)$$

It follows that

$$V = V_0[1 + R_\zeta(\zeta)], \quad (2.31)$$

and

$$N^2 = N_0^2[1 - \gamma R_{\zeta\zeta}(\zeta)]. \quad (2.32)$$

Note that the dimensionless parameter γ determines the magnitude of N^2 in the boundary layer (2.32). As a result, γ (2.29) is inversely proportional to the height of the boundary layer δ, which is defined so that V satisfies (2.25). The role of γ in determining the stratification in the boundary layer will be illustrated further below.

The terms in the coefficients in (2.22) are then

$$(V_x/f) = -S_0\gamma R_{\zeta\zeta}, \quad (2.33a)$$

$$(V_z/f)\tan\alpha = S_0\gamma R_{\zeta\zeta}, \quad (2.33b)$$

$$S = S_0[1 - \gamma R_{\zeta\zeta}], \quad (2.33c)$$

and (2.22) becomes

$$\psi_{\zeta\zeta\hat{t}\hat{t}} = -(1 + S_0)\psi_{\zeta\zeta} + 2S_0\psi_{\zeta\xi} - S_0(1 - \gamma R_{\zeta\zeta})\psi_{\xi\xi}. \quad (2.34)$$

For the dimensionless function $R(\zeta)$, the conditions (2.25), (2.26a,b), and (2.27) require, respectively,

$$R_\zeta(\zeta = 0) = -1, \quad (2.35)$$

$$R_\zeta(\zeta) \to 0, \qquad R_{\zeta\zeta}(\zeta) \to 0 \quad \text{for } \zeta \gg 1, \quad (2.36a,b)$$

and

$$\gamma R_{\zeta\zeta}(\zeta) \leq 1. \tag{2.37}$$

To ensure the satisfaction of (2.37) we require

$$0 \leq \gamma \leq 1 \quad \text{and} \quad R_{\zeta\zeta}(\zeta) \leq 1. \tag{2.38a,b}$$

We will concentrate here primarily on the case where

$$R(\zeta) = R_L(\zeta) = \begin{cases} \frac{1}{2}\zeta^2 - \zeta + \frac{1}{2}, & 0 \leq \zeta \leq 1 \\ 0, & 1 \leq \zeta \end{cases} \tag{2.39}$$

so that

$$R_{L\zeta} = \zeta - 1, \qquad R_{L\zeta\zeta} = 1 \quad \text{for } 0 \leq \zeta \leq 1, \tag{2.40a,b}$$

$$R_{L\zeta} = R_{L\zeta\zeta} = 0 \quad \text{for } 1 \leq \zeta. \tag{2.41a,b}$$

Some of the analysis that follows holds for more general functions R. A simple illustrative example of another function that satisfies (2.35), (2.36a,b), and (2.38b) is

$$R(\zeta) = R_E(\zeta) = \exp(-\zeta). \tag{2.42}$$

The potential vorticity of the basic state specified by (2.31) and (2.32) is

$$\Pi = (f + V_x)\overline{\rho}_z - V_z\overline{\rho}_x \tag{2.43a}$$

$$= (f\rho_0/g)\{-[1 + (V_x/f)]N^2 + f^2(V_x/f)^2\} \tag{2.43b}$$

$$= -(f\rho_0/g)N_0^2[1 - \gamma R_{\zeta\zeta}(\zeta)(1 + S_0)]. \tag{2.44}$$

It follows that

$$\Pi = -f\rho_0 N_0^2/g < 0 \quad \text{for } \zeta \gg 1 \tag{2.45}$$

and that

$$\Pi \gtrless 0 \quad \text{for } \gamma R_{\zeta\zeta} \gtrless (1 + S_0)^{-1}, \tag{2.46a}$$

$$\Pi = 0 \quad \text{for } \gamma R_{\zeta\zeta}(1 + S_0)^{-1}. \tag{2.46b}$$

Considering $R = R_L(\zeta)$ (2.39), we find from (2.33c) that

$$S = S_0(1 - \gamma), \qquad 0 \leq \zeta \leq 1, \tag{2.47}$$

and from (2.44) that

$$\Pi = -(f\rho_0/g)N_0^2[1 - \gamma(1 + S_0)], \qquad 0 \leq \zeta \leq 1. \tag{2.48}$$

The arrested Ekman layer equilibrium solution corresponds to

$$\gamma = 1 \tag{2.49}$$

so that there are no vertical gradients of density in the boundary layer and

$$S = 0, \qquad \Pi = (f\rho_0/g)N_0^2 S_0 > 0, \qquad 0 \leq \zeta < 1. \tag{2.50a,b}$$

The condition of zero potential vorticity,

$$\Pi = 0, \qquad 0 \leq \zeta \leq 1, \tag{2.51}$$

occurs when

$$\gamma = \gamma_C = (1 + S_0)^{-1} \tag{2.52}$$

so that, in the boundary layer,

$$N^2 = N_C^2 = N_0^2(1 - \gamma_C) = N_0^2 S_0(1 + S_0)^{-1}. \tag{2.53}$$

In this case, the boundary layer height δ (2.29) is greater than with $\gamma = 1$, corresponding to the fact that in the basic-state boundary layer the horizontal density gradient, and thus the vertical gradient V_z, is reduced for $\gamma = (1 + S_0)^{-1}$ compared to $\gamma = 1$. We note that if a modified Richardson number is defined as (Bennetts and Hoskins 1979)

$$\mathrm{Ri}_M = [1 + (V_x/f)]\mathrm{Ri}, \qquad \mathrm{Ri} = N^2/V_z^2, \tag{2.54a,b}$$

then

$$\mathrm{Ri}_M = (1 - \gamma)(1 - \gamma S_0)/(\gamma^2 S_0) \tag{2.54c}$$

and $\Pi = 0$ ($\gamma = \gamma_C$) corresponds to $\mathrm{Ri}_M = 1$.

It is of interest to determine the slope of the density surfaces in the basic-state boundary layer:

$$\hat{s} = (\partial z/\partial x)_{\overline{\rho}} = -\overline{\rho}_x/\overline{\rho}_z = -fV_z/N^2 \tag{2.55a}$$

$$= -\gamma(1 - \gamma)^{-1}\tan\alpha. \tag{2.55b}$$

For, $\gamma = 1$, $\hat{s}^{-1} = 0$, as expected, whereas for $\gamma = (1 + S_0)^{-1}$, corresponding to $\Pi = 0$,

$$\hat{s} = \hat{s}_C = -S_0^{-1}\tan\alpha. \tag{2.56}$$

We point out that Allen and Newberger (1996) obtained an approximate estimate for $(\partial z/\partial x)_{\overline{\rho}}$ under similar conditions with $\Pi = 0$ utilizing the assumption $V_x \ll f$. That estimate [denoted by γ and given in Eq. (6.9) there] is not exact. It agrees with the exact result (2.56) only asymptotically for $S_0 \ll 1$ and should be replaced by (2.56).

3. Linear stability analysis

We look for normal mode solutions of (2.34) in the form

$$\psi = \exp(\omega\hat{t} + ik\xi)\phi(\zeta). \tag{3.1}$$

Substituting (3.1) in (2.34) we obtain

$$(1 + S_0 + \omega^2)\phi_{\zeta\zeta} - 2ikS_0\phi_\zeta - k^2S_0(1 - \gamma R_{\zeta\zeta})\phi = 0, \tag{3.2}$$

where we assume $S_0 > 0$, (2.38a,b), and $k \geq 0$. For simplicity, we consider solutions of (3.2) in the domain

$$0 \leq \zeta \leq \zeta_0, \qquad \zeta_0 \gg 1, \tag{3.3}$$

where boundary conditions, corresponding to no normal velocity, are

$$\phi = 0 \quad \text{at} \quad \zeta = 0, \zeta_0. \tag{3.4a,b}$$

Later we will see that the unstable solutions of (3.2) are independent of ζ_0 in the limit $\zeta_0 \to \infty$, justifying the use of the domain (3.3) and boundary condition (3.4b).

It may be readily shown that the eigenvalues ω^2 are

real. Multiply (3.2) by the complex conjugate ϕ^* (denoted by an asterisk), subtract the result of multiplying the conjugate of (3.2) by ϕ, and integrate in ζ over the domain using the boundary conditions (3.4a,b). The result is

$$(\omega^2 - \omega^{2*}) \int_0^{\zeta_0} \phi_\zeta \phi_\zeta^* \, d\zeta = 0, \tag{3.5}$$

which implies

$$\omega^2 = \omega^{2*}. \tag{3.6}$$

If $\omega^2 > 0$, the basic flow is unstable, whereas, if $\omega^2 < 0$, the perturbations consist of stable oscillations.

For further analysis of (3.2), it is useful to define

$$\phi(\zeta) = \exp(ikS_0\lambda\zeta)g(\zeta), \tag{3.7a}$$

$$\lambda = (1 + S_0 + \omega^2)^{-1}, \tag{3.7b}$$

where, from (3.2), g satisfies

$$g_{\zeta\zeta} + g\{k^2S_0\lambda^2[-(1 + \omega^2) + \gamma R_{\zeta\zeta}(1 + S_0 + \omega^2)]\} = 0 \tag{3.8}$$

with boundary condition

$$g = 0 \quad \text{at} \quad \zeta = 0, \zeta_0. \tag{3.9}$$

Multiplying (3.8) by g, integrating in ζ over the domain, and using (3.9) we obtain

$$k^2S_0\lambda^2 \int_0^{\zeta_0} g^2[-(1 + \omega^2) + \gamma R_{\zeta\zeta}(1 + S_0 + \omega^2)] \, d\zeta = \int_0^{\zeta_0} g_\zeta^2 \, d\zeta. \tag{3.10}$$

From (3.10), it is clear that for instability ($\omega^2 > 0$), it is necessary to have

$$\gamma R_{\zeta\zeta}(1 + S_0 + \omega^2) > (1 + \omega^2) \tag{3.11}$$

somewhere in the domain. Satisfaction of (3.11) requires

$$\gamma R_{\zeta\zeta} > [(1 + S_0(1 + \omega^2)^{-1}]^{-1} > (1 + S_0)^{-1}, \tag{3.12}$$

which, from (2.44), implies for instability the necessity of

$$\Pi > 0 \tag{3.13}$$

somewhere in the domain. Condition (3.13) is consistent with the results of Ooyama (1966) and others (e.g., Stone 1966; Bennetts and Hoskins 1979).

We find solutions to (3.2) and (3.3) for ϕ when $R = R_L$ (2.39). Some different basic-state flows are considered in appendix A. For $R = R_L$,

$$S_0(1 - \gamma R_{\zeta\zeta}) = \begin{cases} S_0, & 1 < \zeta \le \zeta_0 \\ S_0(1 - \gamma), & 0 \le \zeta < 1. \end{cases} \tag{3.14}$$

The proper matching conditions at $\zeta = 1$, resulting from continuity in normal mass flux and in pressure, correspond to continuity of ϕ and ϕ_ζ (see also appendix A). It is convenient to utilize (3.7) and solve (3.8) for g. The matching conditions for ϕ likewise imply continuity of g and g_ζ at $\zeta = 1$. We look for solutions with $\omega^2 \ge 0$ and assume $\zeta_0 \to \infty$.

We obtain

$$g = \begin{cases} g_+ = C_0 \exp[-\beta_+(\zeta - 1)], & 1 < \zeta \quad (3.15a) \\ g_- = C_0 \sin(\beta_-\zeta)/\sin(\beta_-), & 0 \le \zeta \le 1, \quad (3.15b) \end{cases}$$

where

$$\beta_+ = kS_0^{1/2}\lambda(1 + \omega^2)^{1/2}, \tag{3.15c}$$

$$\beta_- = kS_0^{1/2}\lambda[-(1 + \omega^2)(1 - \gamma) + \gamma S_0]^{1/2}, \tag{3.15d}$$

and where (3.15a,b) satisfy

$$g_-(\zeta = 0) = 0, \qquad g_+(\zeta \to \infty) \to 0, \tag{3.16a,b}$$

$$g_+(\zeta = 1) = g_-(\zeta = 1). \tag{3.17}$$

Application of the remaining matching condition,

$$g_{+\zeta}(\zeta = 1) = g_{-\zeta}(\zeta = 1), \tag{3.18}$$

gives the relation

$$\tan\beta_- = -\beta_-/\beta_+, \tag{3.19}$$

which determines $\omega^2 = \omega^2(k, S_0, \gamma)$.

Solutions with $\omega^2 \ge 0$, that satisfy (3.16a,b), (3.17), and (3.18), may be found only if

$$\beta_-^2 \ge 0, \tag{3.20}$$

that is, only if

$$[-(1 + \omega^2)(1 - \gamma) + \gamma S_0] \ge 0. \tag{3.21}$$

In that case, an infinite set of solutions of (3.19) exist with

$$\beta_-^2 = \beta_{-n}^2 = a_n^2\pi^2, \qquad \left(n - \frac{1}{2}\right) < a_n < n, \quad n = 1, 2, 3, \cdots. \tag{3.22}$$

The inequality (3.21) implies a bound for ω^2; that is,

$$\omega^2 \le \omega_M^2 = \gamma S_0(1 - \gamma)^{-1} - 1. \tag{3.23}$$

From (3.23), we see that unstable solutions exist, $\omega_M^2 > 0$, only for

$$\gamma > \gamma_C = (1 + S_0)^{-1}, \tag{3.24}$$

that is, for

$$\Pi > 0, \qquad 0 < \zeta \le 1, \tag{3.25}$$

consistent with (3.12) and (3.13).

The substitution of (3.15d) in (3.22) gives

$$\omega^2 = \omega_M^2 - \frac{a_n^2\pi^2(1 + S_0 + \omega^2)^2}{k^2(1 - \gamma)S_0}. \tag{3.26}$$

For $\gamma < 1$, it follows from (3.26) that $d\omega^2/d(k^2) = 0$ for $\omega^2 = \omega_M^2$, which occurs for $k^2 \to \infty$. For $k^2 \gg 1$,

$$\omega^2 \sim \omega_M^2 - \frac{a_n^2\pi^2(1 + S_0 + \omega_M^2)^2}{k^2(1 - \gamma)S_0}. \quad (3.27)$$

Thus, the largest growth rates are found for $n = 1$. The maximum squared growth rate is ω_M^2 and $\omega^2 \to \omega_M^2$ for $k^2 \to \infty$.

For $\gamma = 1$, (3.26) gives

$$\omega^2 = -(1 + S_0) + \frac{kS_0}{a_n\pi}. \quad (3.28)$$

Again, the largest growth rates occur for $n = 1$. The maximum squared growth rate $\omega^2 \to \infty$ for $k \to \infty$.

We note that the maximum squared growth rate ω_M^2 in (3.23) may also be expressed in the form (Stone 1966),

$$\omega_M^2 = (V_z^2/N^2) - 1 = \mathrm{Ri}^{-1} - 1. \quad (3.29)$$

Recalling the scaling (2.19c), we find that the dimensional maximum growth rate scales with $f[\mathrm{Ri}^{-1} - 1]^{1/2}$.

To find $\omega^2 = \omega^2(k)$, we rewrite (3.19) as

$$k = \frac{(1 + S_0 + \omega^2)\tan^{-1}\theta}{S_0^{1/2}[-(1 + \omega^2)(1 - \gamma) + \gamma S_0]^{1/2}}, \quad (3.30a)$$

$$\theta = -\frac{[-(1 + \omega^2)(1 - \gamma) + \gamma S_0]^{1/2}}{(1 + \omega^2)^{1/2}}. \quad (3.30b)$$

For $\omega^2 = 0$, (3.30) gives

$$k = k_C = \frac{(1 + S_0)\tan^{-1}\{-[-(1 - \gamma) + \gamma S_0]^{1/2}\}}{S_0^{1/2}[-(1 - \gamma) + \gamma S_0]^{1/2}}. \quad (3.31)$$

For $\gamma > \gamma_C$, (3.30) implies $\omega^2 \geq 0$ for $k \geq k_C$. Equation (3.30) can be solved directly for $k = k(\omega^2)$. Note that as γ approaches the critical value γ_C, that is, for $\gamma \to \gamma_C$, $k_C \to \infty$, implying that the critical wavenumber for the onset of instability is infinite.

These results are similar to those obtained by Stone (1966, 1970) for inviscid, nongeostrophic, symmetric instabilities in the Eady model. In particular, similar conclusions are found there regarding the infinite critical wavenumber $k_C \to \infty$ for the onset of instability as $\gamma \to \gamma_C$ and also, for a given unstable basic flow with $1 > \gamma > \gamma_C$, regarding the maximum growth rate occurring for $k \to \infty$. These results appear to be general features of inviscid symmetric instability problems. It was originally thought that in the present problem the presence of the length scale δ in the basic flow might result in an inviscid stability analysis giving a finite value of k_C, but that is not the case. To find a finite critical length scale for the onset of symmetric instability in the Eady model, it is necessary to include weak dissipative effects from momentum and density diffusion (Walton 1975). The modification of the inviscid linear stability analysis in the present problem by the introduction of weak dissipative processes is addressed in appendix B.

For the arrested Ekman layer equilibrium basic flow with $\gamma = 1$, (3.31) gives

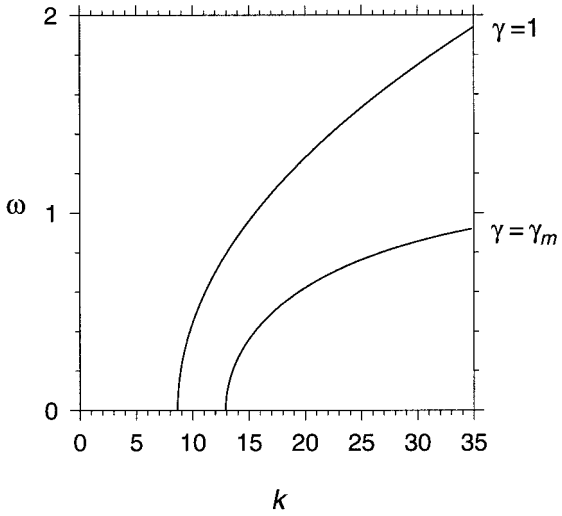

FIG. 1. Results of the inviscid linear stability analysis obtained from (3.30) in terms of growth rates ω of the most unstable mode as a function of wavenumber k with $S_0 = 0.4225$ for $\gamma = 1$ and for $\gamma = \gamma_m = 0.5(1 + \gamma_C)$ where $\gamma_C = (1 + S_0)^{-1}$ (2.52).

$$k_C = [(1 + S_0)/S_0]\tan^{-1}(-S_0^{1/2}), \quad (3.32)$$

where $\omega^2 > 0$ for $k > k_C$ and $\omega^2 \to \infty$ for $k \to \infty$. Growth rates $\omega(k)$ for the most unstable mode ($n = 1$), obtained from the solution to (3.30) are plotted as a function of k for $\gamma = 1$, $S_0 = 0.4225$ in Fig. 1. For comparison, the growth rate $\omega(k)$ for $\gamma = \gamma_m = 0.5[1 + \gamma_C]$ is shown also. It is clear that the arrested Ekman layer equilibrium basic flow with $\gamma = 1$ is linearly unstable to inviscid symmetric instabilities.

With ϕ expressed as (3.7), ψ is

$$\psi = \exp[\omega\hat{t} + ik(\xi + S_0\lambda\zeta)]g(\zeta). \quad (3.33)$$

Thus, ψ has zero values along phase lines with slope

$$d\zeta/d\xi = -(S_0\lambda)^{-1} = -S_0^{-1}(1 + S_0 + \omega^2). \quad (3.34)$$

In terms of the original (x, z) coordinates, the slope of these phase lines is

$$dz/dx \simeq -(1 + S_0 + \omega^2)S_0^{-1}\tan\alpha. \quad (3.35)$$

A comparison of (3.35) with (2.56) shows that for $\omega^2 \ll 1$, $S_0 \ll 1$, the streamlines of the unstable perturbations have a dominant alignment along (x, z) directions with slope $dz/dx \approx \hat{s}_C$, approximately equal to the slope of the density surfaces in the basic-state boundary layer with $\Pi = 0$. In general, the slope of the phase lines $|dz/dx| > \hat{s}_c$.

4. Finite amplitude behavior

To verify the general predictions of the liner stability analysis in section 3 and to investigate finite amplitude nonlinear behavior, we conduct a set of numerical experiments. The experiments involve two-dimensional initial value problems with initial conditions corre-

sponding to the basic-state flows (2.31) and (2.32) with $R = R_L$ (2.39). For $\gamma = 1$, the basic-state flow corresponds to the inviscid, arrested Ekman layer solution. The Blumberg–Mellor (1987) hydrostatic primitive equation, sigma coordinate, finite-difference model is utilized. The model formulation is similar to that described in Allen and Newberger (1996). It involves dimensional variables and includes use of potential density σ_θ in place of temperature and salinity.

With regard to previous investigations of finite amplitude behavior of symmetric instabilities we call attention to the study of Thorpe and Rotunno (1989), who utilize numerical experiments to investigate the nonlinear evolution of atmospherically relevant flows that are initially unstable to symmetric disturbances (see also Miller 1984). The problems considered in those studies differ, however, from the boundary-layer-type flows considered here. On the other hand, the preliminary results reported in Bishop and Chen (1995), regarding the development of two-dimensional finite amplitude symmetric instabilities in baroclinic atmospheric boundary layers, are relevant to the oceanic transient adjustment problem over bottom slope considered by MacCready and Rhines (1993) in a one-dimensional approximation.

To clarify the dependence on dimensionless parameters, we record below the nonlinear equations in dimensionless variables. We also include a simplified representation of the vertical diffusion terms with constant eddy coefficients. For notational simplicity, we utilize the same symbols as for the corresponding dimensional variables in (2.1). The dimensionless variables are formed using the characteristic values [L, H, f^{-1}, V_0, $(H/L)V_0$] for a horizontal length scale, vertical length scale, timescale, horizontal velocity scale, and vertical velocity scale. The pressure is scaled by $p_C = \rho_0 V_0 f L$. The total dimensional density is written as $\rho_T = \rho_0 + \hat{\rho}(z) + \rho'$, where dimensionless $\rho = \rho'/\rho_C$, with $\rho_C = p_C/(Hg)$.

In terms of dimensionless variables, the equations in Cartesian coordinate for two-dimensional flow are

$$u_x + w_z = 0, \tag{4.1a}$$

$$u_t + \mathrm{Ro}\mathbf{u}\cdot\boldsymbol{\nabla}u - v = -p_x + E_M u_{zz}, \tag{4.1b}$$

$$v_t + \mathrm{Ro}\mathbf{u}\cdot\boldsymbol{\nabla}v + u = E_M v_{zz}, \tag{4.1c}$$

$$0 = -p_z - \rho, \tag{4.1d}$$

$$\rho_t + \mathrm{Ro}\mathbf{u}\cdot\boldsymbol{\nabla}\rho + \hat{S}w = E_H\rho_{zz}. \tag{4.1e}$$

The dimensionless parameters $\mathrm{Ro} = V_0/(fL)$, $\hat{S} = N_0^2 H^2/(f^2L^2)$, $E_M = K_M/(fH^2)$, $E_H = K_H/(fH^2)$, where $N_0^2 = -g\hat{\rho}_z/\rho_0$ and where K_M and K_H are the constant vertical turbulent kinematic viscosity and diffusivity coefficients respectively.

For the experiments here with initial conditions corresponding to (2.31), (2.32), and (2.39) with N_0^2 a constant, we further utilize the scaling of section 2 and choose $H = \delta$ and $L = \delta/\tan\alpha$. It follows that

$$\hat{S} = S_0 = (N_0^2/f^2)\tan^2\alpha. \tag{4.2}$$

In addition, in this problem the particular form of the initial conditions results in a relationship (2.29) between V_0, N_0^2, and δ that implies

$$\mathrm{Ro} = V_0/(fL) = V_0\tan\alpha/(f\delta) = \gamma S_0/\cos\alpha \simeq \gamma S_0. \tag{4.3}$$

Thus, if the domain is large enough that the flow is insensitive to the domain-imposed scales for L and H, the inviscid dynamics of this problem depend on the two parameters S_0 and γ. Vertical turbulent diffusion processes add dependence on the parameters E_M and E_H.

The model domain is shown in Fig. 2. It consists of a channel with a uniformly sloping bottom. The across-channel coordinate is x ($0 \le x \le x_0$). The width $x_0 =$ 60 km. The undisturbed depth is $H(x)$. The bottom slope is $\tan\alpha = 0.449 \times 10^{-2}$, which is representative of continental shelves. The bottom has a minimum depth $H_{\min} = 200$ m at $x = x_0$. The depth is greater than 200 m so that in these experiments the flow in the bottom layer will be independent of the upper boundary. No-normal flow, free-slip, and zero density flux conditions are utilized at the sidewalls $x = 0$, x_0 as in Allen and Newberger (1996). The Coriolis parameter $f = 1.036 \times 10^{-4}\ \mathrm{s}^{-1}$. The geometry of the domain and f are held constant while the parameters S_0 and γ are varied. The horizontal grid size is $\Delta x = 0.166$ km. Uniform grid spacing in the vertical σ coordinate is used with 100 sigma levels, where $-1 \le \sigma \le 0$.

Most of the salient features of the finite amplitude flows are illustrated by a few experiments with different values of S_0 and of γ. We include two sets of experiments with two different submodels for the vertical turbulent viscosity and diffusivity. The Richardson-number-dependent parameterization of Pacanowski and Philander (1981, designated P–P) and the Mellor–Yamada (1982) level 2.5 submodel (designated M–Y) with modifications described in Galperin et al. (1988) are utilized as described in Allen and Newberger (1996). The other model parameters have the same values as in the basic case experiment in Allen and Newberger except that here the wind stress forcing is zero and with M–Y the background vertical viscosity and diffusivity $\nu_M = \nu_H = 2 \times 10^{-5}\ \mathrm{m}^2\ \mathrm{s}^{-1}$. The parameters for the experiments are listed in Table 1. Parallel sets of experiments are run with the P–P (experiments 1–5) and with the M–Y (experiments 1M–5M) turbulence parameterizations. Similar results are obtained in comparable experiments as documented below. We choose to concentrate discussion primarily on the experiments using the simpler P–P parameterization to emphasize that the major qualitative features of the results are not dependent on the use of a more complex turbulence closure submodel.

The vertical height of the basic-state boundary layer, utilizing (2.29), is

$$\delta^{(z)} = \delta/\cos\alpha = V_0\tan\alpha(\gamma f S_0)^{-1}. \tag{4.4}$$

In experiments 1–5 we vary N_0^2 (and hence S_0) and also

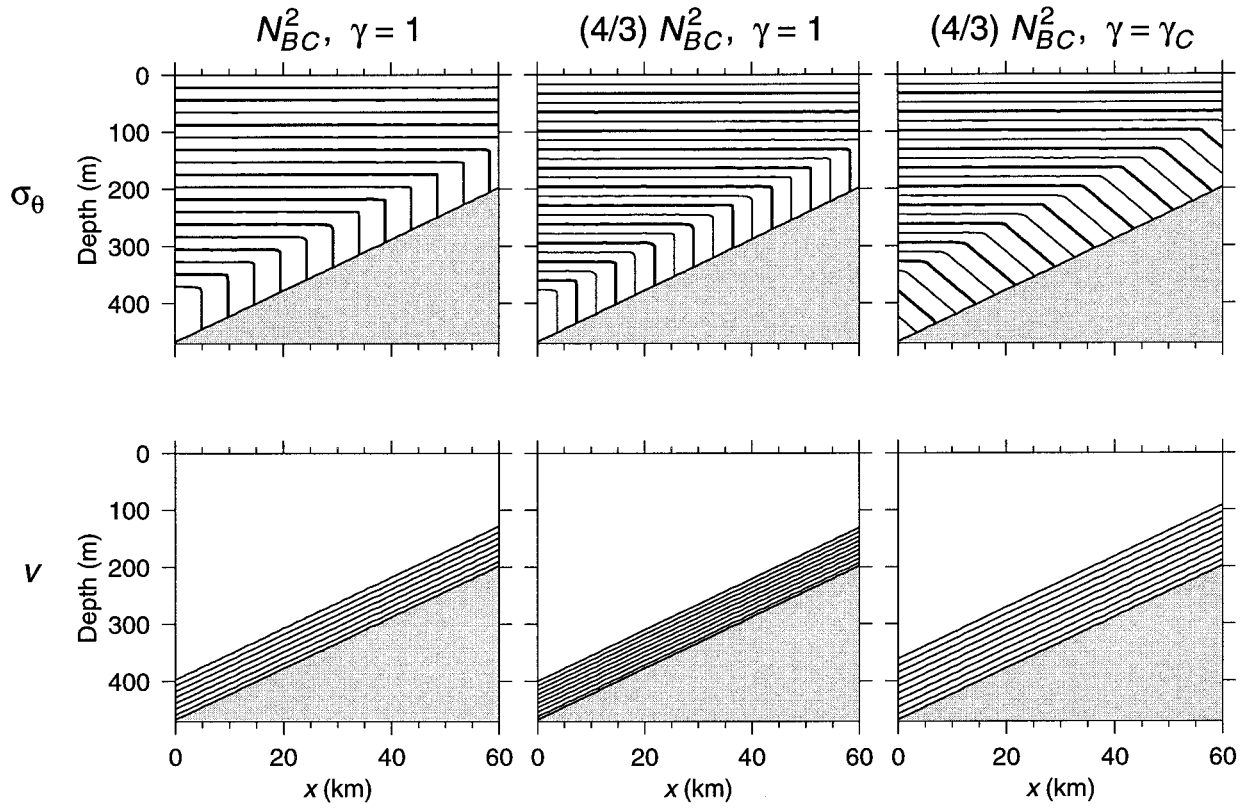

FIG. 2. Initial conditions for the density σ_θ and the alongshore velocity v with $\gamma = 1$ for experiment 2 ($N_0^2 = N_{\rm BC}^2$) and for experiment 3 ($N_0^2 = (4/3)N_{\rm BC}^2$). Also shown in the right column are the σ_θ and v fields corresponding to marginally stable initial conditions for $N_0^2 = (4/3)N_{\rm BC}^2$ with $\gamma = \gamma_C = (1 + S_0)^{-1}$ and $\Pi(t = 0) = 0$ in the boundary layer. The contour intervals are $\Delta\sigma_\theta = 0.5$ kg m^{-3} and $\Delta v = 0.1$ m s^{-1} with $v = 0$ at the bottom.

V_0 so that, for fixed γ, $\delta^{(z)}$ remains the same ($\delta^{(z)} = \gamma^{-1}$ 76.9 m). Experiment 2 in Table 1 with $N_0^2 = N_{\rm BC}^2 = 2.25 \times 10^{-4}$ s^{-2} and $V_0 = 0.75$ m s^{-1} may be thought of as the basic case experiment. To help initiate flow instabilities, small x-dependent perturbations at wavelengths λ_H, where $\lambda_{H_{\rm min}} \le \lambda_H \le x_0$, are added to the depth H. In experiments 1–7, 30 equal-amplitude Fourier components with random phases are utilized so that $\lambda_{H_{\rm min}} = 2$ km. The amplitudes of the modes are scaled so that the maximum total amplitude variation in H is $\Delta H = 1$ m. The effects of using different bottom topographic perturbations are investigated in experiments 1A–3A and 1B–3B as described later in this section.

TABLE 1. Summary of parameter values for the primary set of numerical experiments with the P–P turbulence parameterization scheme. Experiments 1M–5M have the same parameters as experiments 1–5, respectively, but utilize the M–Y turbulence closure model. Experiments 1A–3A and 1B–3B have the same parameters as experiments 1–3, respectively, but have different bottom topographic perturbations as explained in section 4. $N_{\rm BC}^2 = 2.25 \times 10^{-4}$ s^{-2}, $\gamma_m = 0.5(1 + \gamma_C)$, where $\gamma_C = (1 + S_0)^{-1}$.

Expt	S_0	N_0^2 (s^{-2})	V_0 (m s^{-1})	γ
1	0.2816	$(2/3)N_{\rm BC}^2$	0.5	1
2	0.4225	$N_{\rm BC}^2$	0.75	1
3	0.5633	$(4/3)N_{\rm BC}^2$	1.0	1
4	0.4225	$N_{\rm BC}^2$	0.75	γ_m
5	0.5633	$(4/3)N_{\rm BC}^2$	1.0	γ_m
6	0.4225	$N_{\rm BC}^2$	1.0	1
7	0.4225	$N_{\rm BC}^2$	0.75	$0.95\gamma_C$

The initial conditions for experiments 1–3 correspond to the arrested Ekman layer equilibrium flow with $\gamma = 1$ and thus with $\sigma_{\theta z}(t = 0) = 0$ in the boundary layer. The initial conditions for σ_θ and v for experiments 2 and 3 are shown in Fig. 2. The initial condition for the velocity component u is zero. Also shown in Fig. 2 for comparison and for later reference are the initial σ_θ and v fields for the same S_0 value as in experiment 3, but for the marginally stable situation where $\Pi(t = 0) = 0$ and $\gamma = \gamma_C = (1 + S_0)^{-1}$ in the boundary layer.

It is perhaps useful to mention at the outset the results of experiment 7 (Table 1) where the parameters are the same as experiment 2 except that $\gamma = 0.95\gamma_C$. Since $\gamma < \gamma_C$, this flow should be stable by the linear stability theory results of section 3. In experiment 7, the basic-state flow is found to remain essentially steady and undisturbed as predicted by the linear analysis. Some very small flow perturbations were observed in the bottom

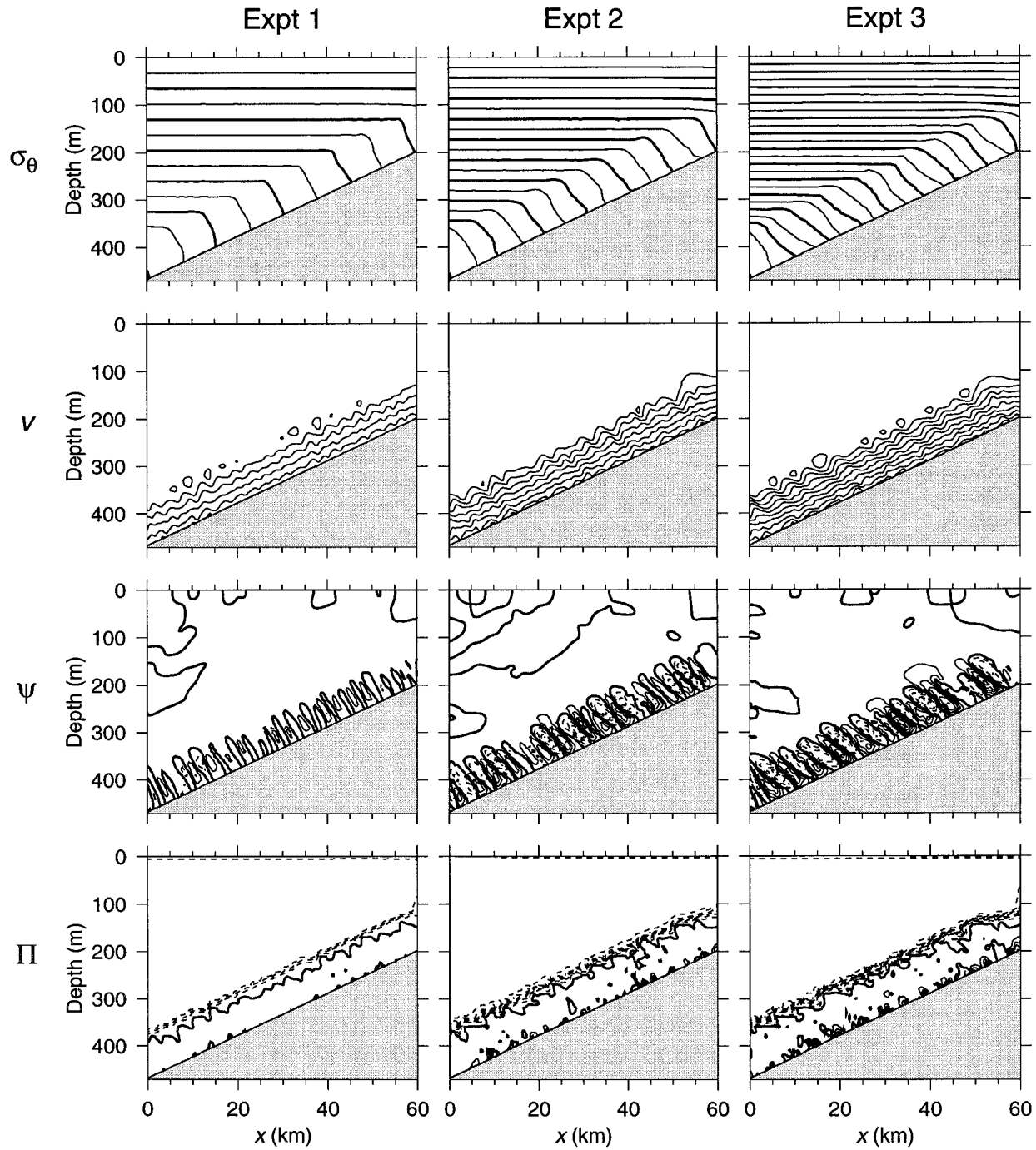

FIG. 3. Fields at day 4 of the density σ_θ, the alongshore velocity v, the streamfunction ψ, and the potential vorticity Π (4.5) from experiment 1 ($N_0^2 = (2/3)N_{BC}^2$), experiment 2 ($N_0^2 = N_{BC}^2$), and experiment 3 ($N_0^2 = (4/3)N_{BC}^2$). All variables are averaged over an inertial period. The contour intervals $\Delta\sigma_\theta = 0.5$ kg m^{-3}, $\Delta v = 0.1$ m s^{-1}, $\Delta\psi = 0.2$ m^2 s^{-1}, where $\psi = 0$ is marked with a heavy line and $\psi > 0$ is dashed and $\Delta\Pi = 5 \times 10^{-7}$ kg m^{-4} s^{-1}, where $\Pi = 0$ is marked with a heavy line and $\Pi < 0$ is dashed.

boundary layer, presumably as a result of the fact that the initial density field does not satisfy the bottom boundary condition $\partial\sigma_\theta/\partial z = 0$ utilized in the model with vertical density diffusion (Allen and Newberger 1996). The fact that only extremely small flow perturbations are found in this experiment indicates that flow generation related to vertical density diffusion near the bottom boundary is relatively unimportant in these experiments.

The fields of σ_θ, v, ψ, and Π from experiments 1, 2,

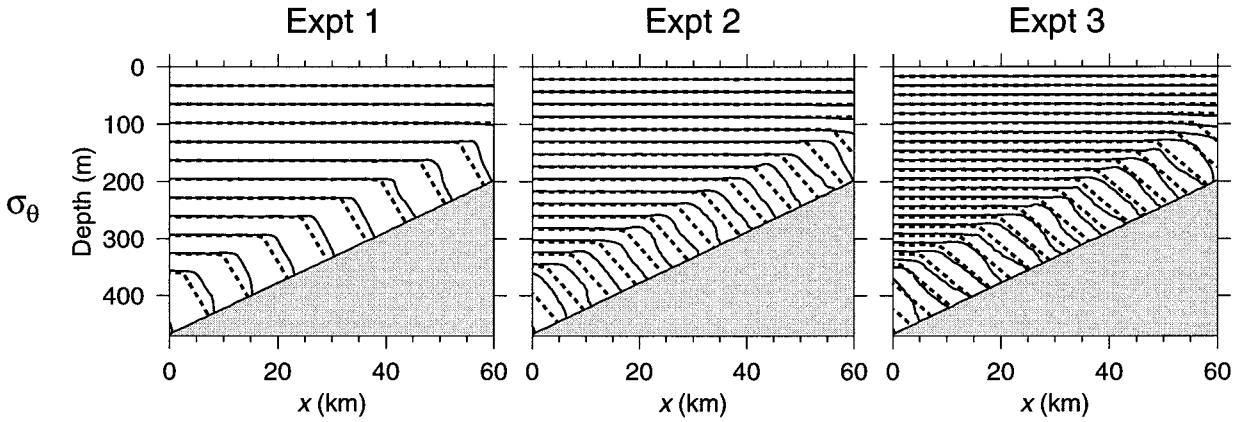

FIG. 4. Fields of σ_θ at day 4 from experiments 1, 2, and 3 (solid lines) with fields of σ_θ corresponding to marginally stable initial conditions [$\gamma = \gamma_C = (1 + S_0)^{-1}$ and $\Pi(t = 0) = 0$ in the boundary layer] for these experiments (dashed lines) superposed. The variables at day 4 have been averaged over an inertial period. The contour interval is $\Delta\sigma_\theta = 0.5$ kg m^{-3}.

and 3 at day 4 are shown in Fig. 3, where ψ is the (approximate) streamfunction for u and w (2.12) calculated as described in Allen and Newberger (1996) and Π is the potential vorticity,

$$\Pi = (f + v_x)\sigma_{\theta z} - v_z\sigma_{\theta x}. \tag{4.5}$$

The variables in these fields have been averaged over an inertial period to remove the effects of high-frequency waves and to clarify the subinertial frequency response. It is obvious that the initial flow fields are unstable and that the flow has evolved in time. The slopes

$$s = (\partial z/\partial x)_{\sigma_\theta} = -\sigma_{\theta x}/\sigma_{\theta z} \tag{4.6}$$

of the density surfaces in the boundary layer have changed from the initial conditions, where $s^{-1}(t = 0) = \hat{s}^{-1} = 0$, to values that vary with (x, z, t). As may be seen clearly in Fig. 4, where the initial σ_θ fields for $\gamma = \gamma_C$ are superposed on the day 4 σ_θ fields from Fig. 2, the day 4 values of s are generally close to those for the condition of marginal stability $\Pi = 0$; that is, $s \simeq \hat{s}_C = -S_0^{-1}\tan\alpha$. Correspondingly, the day 4 values of Π in the bottom boundary layer show some spatial variability, but are appreciably closer to $\Pi = 0$ than they are in the initial fields as will be illustrated more clearly below.

The most striking aspect of the day 4 flow fields appears in the streamfunction ψ and is the presence in the bottom boundary layer of periodic circulation cells. The circulation cells are slanted such that the dominant direction of the flow is generally aligned along the density surfaces. One obvious difference in the day 4 fields from experiments 1–3 is that the slope of the density surfaces $|s|$ (4.6), and of the circulation cells, decreases as N_0^2 increases. This fact is in agreement with the observation above that $s \simeq \hat{s}_C$. Another clear difference is that the horizontal length scales of the cells increase as V_0 increases. The horizontal scales of the circulation cells will be discussed further below.

The v fields (Fig. 3) also show the horizontal and vertical variability associated with the circulation cells. This is especially clear in experiment 3. The semiregular ripples in the v contours have a vertical phase variation such that the crests and troughs are aligned along the dominant direction of the zero ψ contours. This structure evidently reflects the advective effects from u and w on v since the crests (troughs) of v are aligned along the vertically ascending (descending) flow.

For comparison, the day 4 ψ fields from experiments 1M–3M with the M–Y turbulence closure scheme are shown in Fig. 5. The qualitative similarity with the day 4 ψ fields from the corresponding experiments 1–3 with the P–P turbulence parameterizations (Fig. 3) is evident. A more quantitative comparison is given below.

An illustration of the time variability of the flow is provided by a contour plot of the across-shelf velocity u near the bottom ($\sigma = -0.945$) as a function of x and t from experiment 3 (Fig. 6). This plot also provides additional information on the horizontal scale of the circulation cells. Evidence for the formation of horizontally periodic circulation cells is visible from the variations in sign of u after about 1.5 days. A tendency for these cells to propagate upslope toward positive x, as found in the downwelling experiments in Allen and Newberger, is also evident. The propagating velocities are variable, but after day 3 appear to be around 1 km/day. Quantitative estimates for the dominant horizontal scale are obtained from spectra calculated from these values of $u(x, t)$. Normalized spectra from experiments 1–3 and 1M–3M at day 8 are shown in Fig. 7. We choose day 8 because, as seen in Fig. 6, the horizontal scales become somewhat more regular at larger time and identification of a single dominant scale from the spectra is facilitated. In addition, since the initial flow is unstable and therefore somewhat artificial, we do not place strong emphasis on the details of the adjustment process at short time. The dominant horizontal wavelengths λ_D for experiments 1, 2, and 3 at day 8

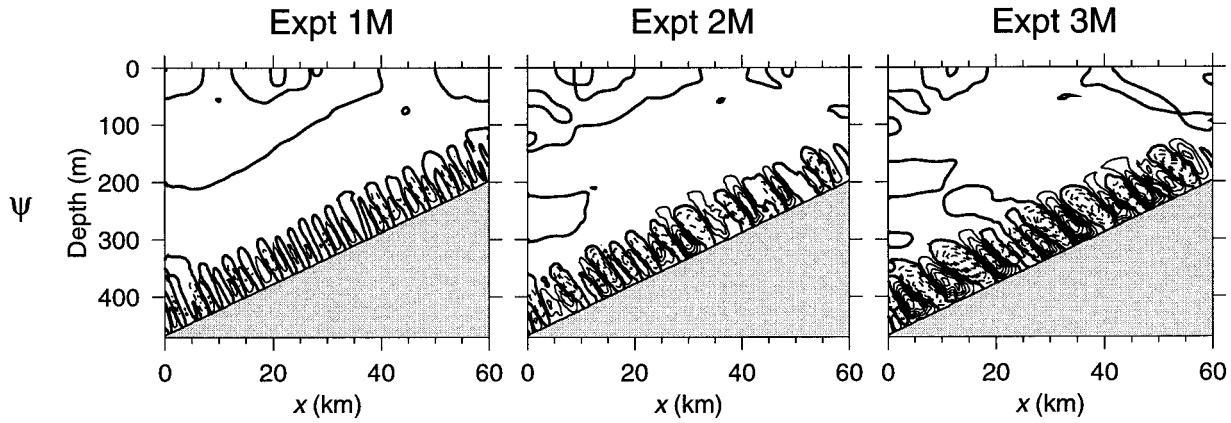

FIG. 5. Fields of ψ at day 4 from experiments 1M, 2M, and 3M with the Mellor–Yamada (M–Y) level 2.5 turbulence closure scheme. The variables have been averaged over an inertial period. The contour interval is $\Delta\psi = 0.2$ m^2 s^{-1}, where $\psi = 0$ is marked with a heavy line and $\psi > 0$ is dashed.

from the spectra in Fig. 7 are given in Table 2 and are 2.84, 3.56, and 4.74 km, respectively. For the corresponding experiments 1M, 2M, and 3M with the M–Y turbulence scheme, the values, also given in Table 2, are 2.67, 3.56, and 4.74 km, which are close to the values found in experiments 1, 2, and 3.

Based on the results in Fig. 4 concerning the slope of the density surfaces, a horizontal length scale $\delta^{(x)}$ may be estimated (Emanuel 1979) from $\hat{s}_C$ (2.56) and $\delta_C^{(z)}$ [where $\delta_C^{(z)} = \delta^{(z)}$ as given in (4.4) with $\gamma = \gamma_C = (1 + S_0)^{-1}$],

$$\delta^{(x)} = -\delta_C^{(z)}\hat{s}_C^{-1} = (V_0/f)(1 + S_0). \qquad (4.7)$$

The scaling dependence of $\delta^{(x)}$ on (V_0/f) in (4.7) is characteristic of estimates for horizontal scales in slantwise convection (e.g., Emanuel 1994). The expression (4.7) appears to provide a reasonable estimate for the scaling dependence, but not the exact magnitude, of the horizontal scales observed in the finite amplitude flows in these experiments. A calculation of the scale estimate (4.7) for experiments 1, 2, and 3 gives $\delta^{(x)}(1) = 6.2$ km, $\delta^{(x)}(2) = 10.3$ km, and $\delta^{(x)}(3) = 15.1$ km, which are larger values than found in the experiments (Fig. 7). Nevertheless, a calculation of the ratio of the scale estimate (4.7) for experiment 1 to that for experiment 2 gives $\delta^{(x)}(1)/\delta^{(x)}(2) = 0.60$, while for experiments 2 and 3, $\delta^{(x)}(2)/\delta^{(x)}(3) = 0.68$. These are in qualitative agreement with the observed ratios, utilizing the wavelengths from the spectra in Fig. 7, of 0.80 and 0.75, respectively. For experiments 1M, 2M, and 3M, where likewise $\delta^{(x)}(1M)/\delta^{(x)}(2M) = 0.60$ and $\delta^{(x)}(2M)/\delta^{(x)}(3M) = 0.68$, the observed ratios are both 0.75, which similarly agree qualitatively with the ratios from (4.7). We note that the results of the linear stability analysis for inviscid flows in section 3 provide little help for the identification of a likely horizontal scale at finite amplitude. The inclusion of dissipative effects in the linear stability analysis in appendix B, however, provides some support for the (V_0/f) scaling in (B.20b) and in (B.29), as emphasized by Emanuel (1979). The prediction in appendix B for the wavelength $\lambda_M^{(x')}$ of maximum growth rate (B.29) for $\lambda \to 1$ is the same as the inviscid result, that is, $\lambda_M^{(x')} \sim 0$, and thus also is not directly applicable.

A contour plot of σ_θ near the bottom ($\sigma = -0.985$) as a function of x and t (Fig. 8) from experiment 3 shows the formation, after about 1.5 days, of regularly spaced regions in x that have relatively large horizontal gra-

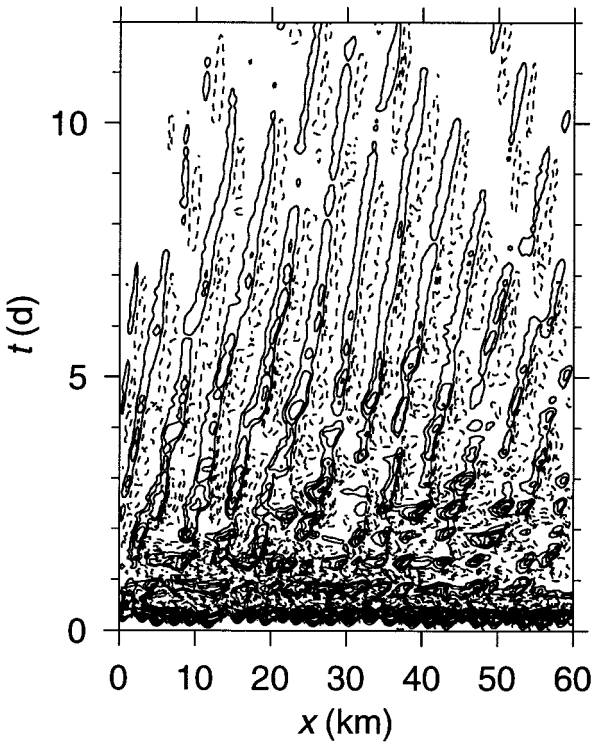

FIG. 6. Contours of the across-shelf velocity u near the bottom ($\sigma = -0.945$) as a function of x and t from experiment 3 with $N_0^2 = (4/3)N_{BC}^2$. The contour interval is $\Delta u = 0.03$ m s^{-1}. Solid (dashed) contour lines correspond to positive (negative) values and the zero contour is omitted.

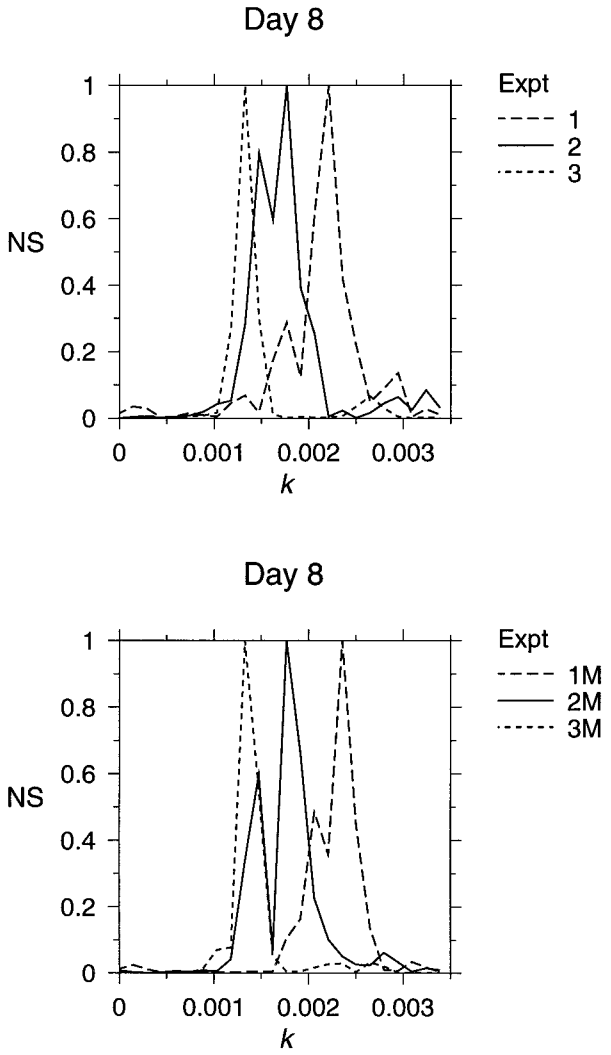

FIG. 7. Normalized power spectra NS for the across-shelf velocity $u(x, \sigma, t)$ near the bottom at $\sigma = -0.945$ and at $t = 8$ d as a function of the x wavenumber k (m^{-1}) for experiments 1, 2, and 3 (top) and for experiments 1M, 2M, and 3M (bottom). The spectra are calculated from the u values at 8.67 km $\leq x \leq$ 51.33 km and are normalized by the maximum spectral values. The corresponding wavelengths $\lambda_D = (2\pi/k)$ at which the spectral peaks occur are listed in Table 2.

dients. These regions reflect advective effects related to the convergence of the near-bottom across-shelf velocity u in the circulation cells. They consequently show the same horizontal scales and the same tendency to propagate upslope toward positive x as seen in the near-bottom $u(x, t)$ plots in Fig. 6.

Additional information about the time variability of the flow in experiment 2 as a function of the depth z may be obtained from contour plots of u, v, and σ_θ as a function of z and t at $x = x_0/2 = 30$ km [$H(x_0/2) = 335$ m] plotted in Fig. 9. Also shown in Fig. 9 for comparison are the corresponding plots from experiment 2M with the M–Y turbulence parameterization. Note the general similarity in behavior in experiments 2 and 2M.

TABLE 2. Wavelengths λ_D (km) of the spectral peaks of $u(x, \sigma, t)$ near the bottom ($\sigma = -0.945$) at day 8 from different experiments.

Expt	λ_D	Expt	λ_D	Expt	λ_D	Expt	λ_D
1	2.84	1M	2.67	1A	3.05	1B	3.28
2	3.56	2M	3.56	2A	4.27	2B	4.74
3	4.74	3M	4.74	3A	5.33	3B	5.33
4	4.27	4M	4.27				
5	5.33	5M	5.33				
6	4.74						

The across-shelf velocity u in the bottom boundary layer shows high-frequency near-inertial oscillations at the outset between $t = 0$ and $t = 1.5$ days. This is followed by the subsequent development after day 1.5 of organized behavior involving fluctuations in both z and t of u about zero. The contours of the u fluctuations have positive slope in the (z, t) plane. The fluctuations are characterized by a timescale of about 3 days and a vertical scale of about 70 m. This variability with z and t reflects the slantwise nature of the circulation cells in x and z seen in the ψ fields in Fig. 3 and the propagation upslope toward positive x of these cells seen in Figs. 6 and 8. The contours of v show the advective effects of the circulation cells in a manner similar to that seen in the day 4 v fields in Fig. 3. The values of v increase and decrease with time at a given z level. The occurrence of the increased values coincides with positive fluctu-

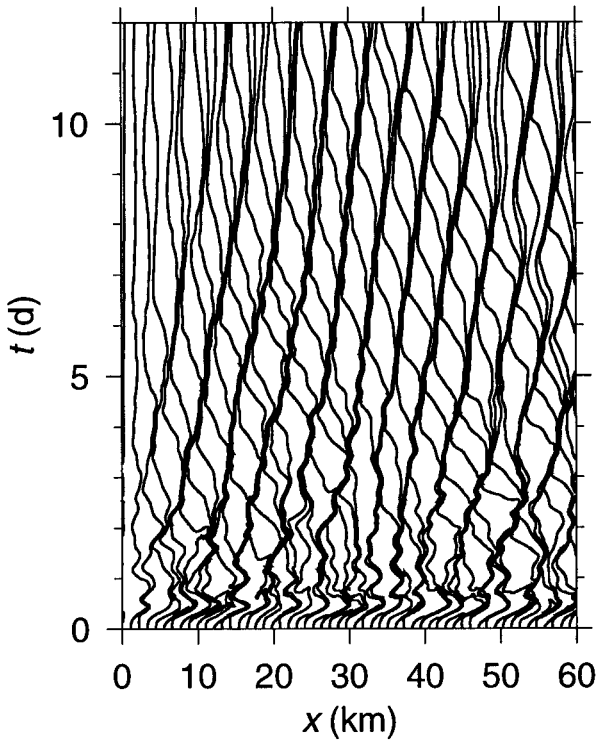

FIG. 8. Contours of density σ_θ near the bottom ($\sigma = -0.985$) as a function of x and t from experiment 3 with $N_0^2 = (4/3)N_{BC}^2$. The contour interval is $\Delta\sigma_\theta = 0.15$ kg m^{-3}.

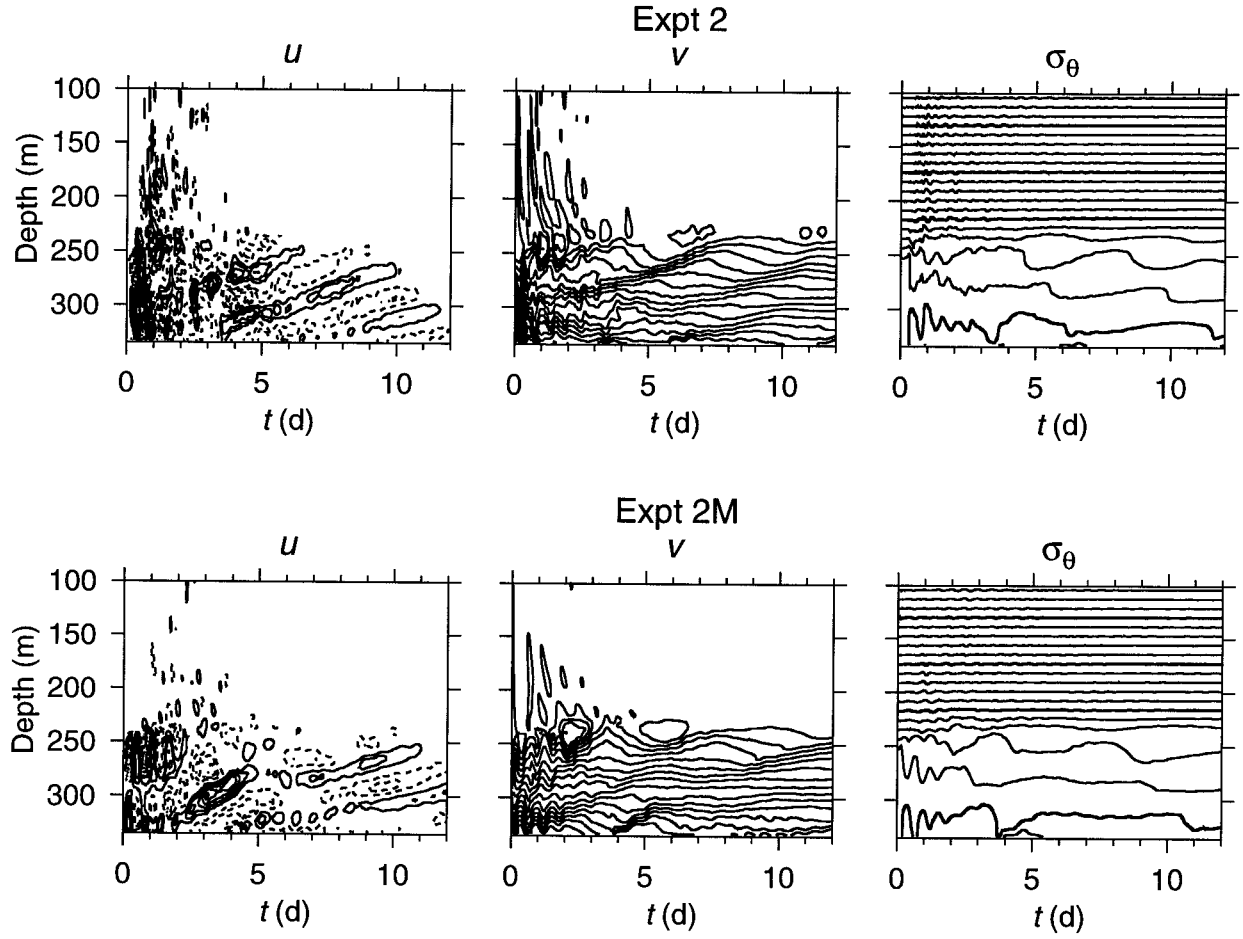

FIG. 9. Contours of u, v, and σ_θ as a function of depth z and of t at $x = 0.5x_0$ from experiment 2 (top) and from experiment 2M with the M–Y turbulence parameterization (bottom). The contour intervals are $\Delta u = 0.02$ m s^{-1} where solid (dashed) contour lines correspond to positive (negative) values and the zero contour is omitted, $\Delta v = 0.05$ m s^{-1} and $\Delta\sigma_\theta = 0.2$ kg m^{-3}.

ations in u, which corresponds to descending motion in the circulation cells. An important feature clearly evident in this plot of v is the increase in height of the boundary layer with time from an initial value of about 80 m to a height that, after about day 3, fluctuates around 100 m.

The contours of density σ_θ in Fig. 9 show the development from the initial condition where $\sigma_{\theta z} = 0$ in the boundary layer, to a condition of continuous density variation in z that is weak compared to the interior but stable with $\sigma_{\theta z} < 0$. The time- and space-dependent advective effects of the circulation cells show up in the σ_θ variability in a manner somewhat similar to that described above for v. The general increase in height of the boundary layer is also clearly evident in the σ_θ contours. We note also the appearance near the bottom of fluid with density greater than in the initial vertical profile of σ_θ at $x = x_0/2$. This occurs as a result of the adjustment of the σ_θ field near the bottom (Fig. 8) so that slopes of the σ_θ surfaces have values $s \simeq s_C$ (Fig. 4).

The potential vorticity Π (4.5) is uniform and is positive in the boundary layer at $t = 0$ with a constant value given by (2.50b). Time series of Π at $x \equiv x_0/2$ and various z levels (Fig. 10) from experiment 2 show the tendency of Π in this region to decrease from the initial condition toward values that remain variable in time but are considerably closer to the zero value characteristic of marginal stability.

The time variations of the volume-integrated kinetic, potential, and total energies for experiment 2 are shown in Fig. 11. The integrated kinetic energy (divided by ρ_0) is calculated here from

$$\mathrm{KE} = \frac{1}{x_0}\int_0^{x_0}\int_{-H}^{\eta}\frac{1}{2}(u^2 + v^2)\,dx\,dz, \qquad (4.8)$$

while the corresponding integrated potential energy is calculated from

$$\mathrm{PE} = \frac{1}{\rho_0 x_0}\int_0^{x_0}\int_{-H}^{\eta} gz\sigma_\theta\,dx\,dz, \qquad (4.9)$$

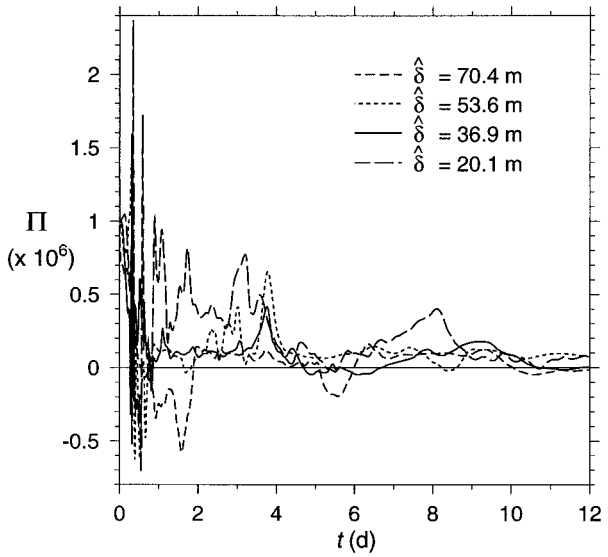

FIG. 10. Time series from experiment 2 of the potential vorticity Π (4.5) (kg m^{-4} s^{-1}) at $x = 0.5x_0$ and at different depths near the bottom designated by the z distance $\hat{\delta}$ above the bottom where $\Pi(t = 0) = 1.0 \times 10^{-6}$ kg m^{-4} s^{-1}.

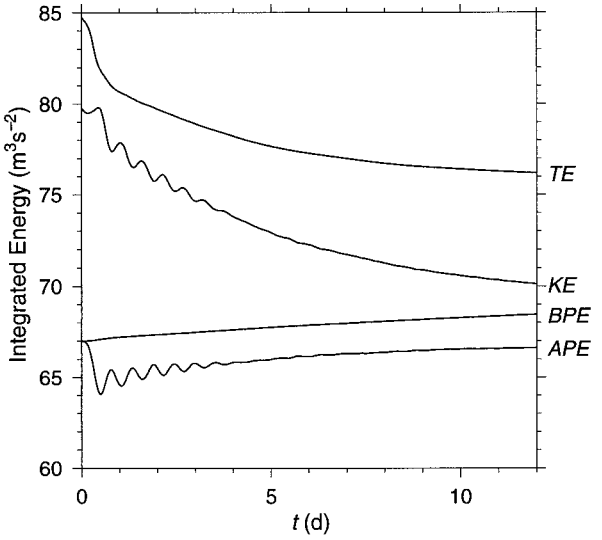

FIG. 11. The integrated kinetic energy KE (4.8), background potential energy BPE (4.12), available potential energy APE (4.11), and total energy TE (4.10) as a function of t from experiment 2. Constants here have been added to the BPE and APE terms so that at $t = 0$, they are equal to 67 m^3 s^{-2}. Another constant has been subtracted from TE so that, for the plot, TE = KE + BPE + APE − 129 m^3 s^{-2}.

where η is the free-surface displacement (Allen and Newberger 1996). The total energy TE is

$$\text{TE} = \text{KE} + \text{PE}. \tag{4.10}$$

It is convenient to further divide the potential energy into background potential energy BPE and available potential energy APE (Winters et al. 1995), so that

$$\text{PE} = \text{BPE} + \text{APE}. \tag{4.11}$$

The background potential energy BPE is defined (Winters et al. 1995) as the minimum potential energy found through an adiabatic redistribution of σ_θ. Changes in potential energy due to diabatic processes are reflected as changes in BPE. Thus, here

$$\text{BPE} = \frac{1}{\rho_0 x_0}\int_0^{x_0}\int_{-H}^{\eta} gz^*\sigma_\theta \, dx \, dz, \tag{4.12}$$

where z^* is the reference position in the state of minimum potential energy of the fluid element at (x, z, t) with density $\sigma_\theta(x, z, t)$. BPE is calculated following Winters et al. (1995) and APE is then obtained from (4.11).

The qualitative features of the energy variability shown in Fig. 11 are typical of all of the experiments in Table 1. The total energy TE decreases with time as a result of dissipative processes. The kinetic energy KE increases slightly initially but then, after half a day, decreases with time. The background potential energy BPE increases slowly with time due to mixing processes. The available potential energy APE decreases initially during a short initial adjustment period of about half a day. After that, as the circulation cells start to develop, APE increases with time. It thus appears that the kinetic energy of the basic state is the major energy source for the finite amplitude symmetric instabilities.

We point out relevant results from experiments 4 and 5. These experiments are initialized with the same parameters as in experiments 2 and 3 except that $\gamma = \gamma_m = (\gamma_C + 1)/2$. Thus, the initial conditions are closer to stable conditions. Qualitative behavior similar to that found in experiments 2 and 3 is observed. In particular, circulation cells develop in a like manner. Similar results are found in the corresponding experiments 4M and 5M with the M–Y turbulence closure scheme. Compared to the flows with $\gamma = 1$, the strengths of the circulation cells are somewhat reduced. In addition, the horizontal scales are generally larger. Spectral calculations of near-bottom $u(x, t)$ from experiments 4 and 5 (and 4M and 5M) indicate that the dominant wavelengths λ_D at day 8 for experiments 4 and 5 (and for 4M and 5M) are 4.27 and 5.33 km (Table 2). These are larger than the wavelengths of 3.56 and 4.74 km found at day 8 in experiments 3 and 4 (and in 3M and 4M). Nevertheless, the variations of the observed wavelengths with experiment, $\lambda_D(4)/\lambda_D(5) = \lambda_D(4M)/\lambda_D(5M) = 0.80$, still agree qualitatively with the scaling estimate (4.4), which predicts a ratio of 0.68.

We check the implications of the arguments at the beginning of this section regarding dependence on the dimensionless parameters S_0 and γ in experiment 6 where $S_0 = 0.4225$ and $\gamma = 1$ (as in expt 2), but $V_0 = 1$ m s^{-1} so that, from (4.4), $\delta^{(z)} = 102.5$ m. For the parameter values of experiments 2 and 6, the nondimensionalization, and also the scaling estimate (4.7), imply that the ratio of horizontal scales $\delta^{(x)}(6)/\delta^{(x)}(2) =$

$V_0(6)/V_0(2) = 1.33$. In the experiment, we find (Table 2) $\lambda_D(6)/\lambda_D(2) = 1.33$, which is in good agreement and is thus consistent with the implications of the nondimensionalization. We can also compare the results of experiments 6 and 3 where $V_0 = 1$ m s^{-1} for both, but S_0 differs. The ratio of observed dominant horizontal scales (Table 2) is $\lambda_D(6)/\lambda_D(3) = 1$, which compares reasonably well with the ratio of scale estimates (4.7) $\delta^{(x)}(6)/\delta^{(x)}(3) = 0.91$.

We also check the effects on the resultant finite amplitude flow of using different bottom topographic perturbations. Experiments 1A–3A have the same parameters as experiments 1–3 except that different random phases are utilized in the 30 bottom perturbation Fourier components. Similar qualitative behavior is found, but the dominant horizontal scales λ_D are larger in experiments 1A–3A (Table 2). The ratio of observed horizontal scales $\lambda_D(1A)/\lambda_D(2A) = 0.71$ and $\lambda_D(2A)/\lambda_D(3A) = 0.80$ are in qualitative agreement with the scaling predictions of (4.7), which, as noted before, are 0.6 and 0.68.

In experiments 1B–3B, the topographic perturbations are again varied. In these experiments, 45 equal-amplitude Fourier components are used so that $\lambda_{H_{\min}} = 1.33$ km, with the first 30 components the same as in experiments 1–3. The qualitative finite amplitude behavior found in experiments 1B–3B is the same as in experiments 1–3, but the dominant horizontal scales are larger in experiments 1B–3B (Table 2). The latter point is noteworthy because the added topographic perturbations at smaller wavelength in experiments 1B–3B do not result in smaller horizontal scales for the finite amplitude circulation cells as might be anticipated based on the results of linear stability theory. Again, the ratio of observed horizontal scales (Table 2) $\lambda_D(1B)/\lambda_D(2B) = 0.69$ and $\lambda_D(2B)/\lambda_D(3B) = 0.89$ are in qualitative agreement with the scaling predictions of (4.7).

The primary conclusions from comparison of the results of experiments 1A–3A, 1B–3B, and 1–3 is that, although qualitative aspects of the corresponding finite amplitude flows are similar, quantitative measures, such as the resulting dominant horizontal scale, are dependent on the details of the topographic perturbations. Results that appear robust include the tendency for the slopes of the density surfaces in the bottom layer to have the same general alignment as those for marginal stability, that is, for $s \approx \hat{s}_C = -S_0^{-1}\tan\alpha$, and the tendency for the resultant dominant horizontal scales, for fixed topographic perturbations, to vary with V_0 in qualitative agreement with the scaling estimate (4.7).

5. Summary

The two primary objectives of this study, as stated in the introduction, are 1) to formulate and examine the stability of an idealized near-bottom flow with conditions dynamically similar to those in the downwelling circulation and 2) to establish a link between the symmetric instabilities observed in the wind-forced downwelling experiments (Allen and Newberger 1996) and the results of recent theoretical studies of bottom boundary layer behavior in stratified oceanic flows over sloping topography (Trowbridge and Lentz 1991; MacCready and Rhines 1993; Garrett et al. 1993).

The first objective is addressed by analyzing the inviscid (section 3) and the weakly dissipative (appendix B) linear stability of the inviscid, arrested Ekman layer solution (Trowbridge and Lentz 1991; MacCready and Rhines 1993; Garrett et al. 1993). It is confirmed that a necessary condition for inviscid, linear, symmetric instability of this type of flow is that the potential vorticity $\Pi > 0$ somewhere in the bottom layer. The inviscid arrested Ekman layer solution with $\gamma = 1$, for which $\Pi > 0$ in the bottom boundary layer, is shown to be linearly unstable by direct calculation of growth rates. The critical wavenumber for onset of instability as $\gamma \to \gamma_C$ and the maximum growth rate for $\gamma_C < \gamma < 1$, are both found to occur at infinite wavenumber, similar to previous results of Stone (1966) for inviscid, nongeostrophic symmetric instabilities in the Eady model. Analysis of the inviscid linear stability of a bottom layer with vertically uniform density, but with a possible jump in density at the top of the bottom layer (appendix A), gives qualitatively similar linear stability characteristics. The addition of weak dissipative effects (appendix B), following the approach of Walton (1975), results in determination of a finite critical wavenumber (B.18) as $\gamma \to \gamma_C$. The resulting critical dimensional wavelength (B20) scales with V_0/f. For $\gamma_{\rm CD} < \gamma < 1$ with weak dissipation, we also determine a finite wavelength $\lambda_M^{(x')}$ (B.29) for maximum growth rate that also scales with V_0/f. For $\lambda \to 1$, however, $\lambda_M^{(x')} \sim 0$, similar to the inviscid result.

The second objective is addressed by conducting numerical experiments to find the finite amplitude behavior resulting when the σ_θ and v fields are initialized with the inviscid, arrested Ekman layer solutions. Those initial conditions are found to be unstable as expected from the linear stability analysis. In the bottom boundary layer, periodic circulation cells form and the density develops weak stable stratification such that the slopes of the σ_θ surfaces are close to those for marginally stable conditions where the potential vorticity $\Pi = 0$ and, correspondingly, where $N^2 \simeq N_C^2$ (2.53). The potential vorticity Π in the bottom layer remains variable in time and space but generally decreases to values near zero. The circulation cells tend to align along the density surfaces so that the motion is primarily slantwise. As S_0 increases, the slope $|s|$ of the density surface (4.6) decreases, consistent with the variation with S_0 of the slopes $\hat{s}_C$ (2.56) at marginal stability with $\Pi = 0$.

The variation of the dominant horizontal scale $\delta^{(x)}$ of the circulation cells is found to be in qualitative agreement with the scaling (4.7), which implies that $\delta^{(x)} \approx V_0/f$. This scaling for $\delta^{(x)}$ is characteristic of estimates for horizontal scales in slantwise convection (Emanuel

1994). Results of linear stability theory do not appear to be of direct applicability in predicting the resulting horizontal scales of the finite amplitude flows [other than the V_0/f scaling dependence found for $\lambda_I^{(x')}$ in (B.20b) and for $\lambda_M^{(x')}$ in (B.29)]. The exact dynamics that govern the horizontal scale selection for the finite amplitude circulation cells remain to be determined. Nevertheless, the slantwise circulation cells found here bear a strong resemblance to those found in the near-bottom flows of the wind-forced downwelling problem (Allen and Newberger 1996). Thus, the present experiments show that the inviscid arrested Ekman layer solution is unstable and that the finite amplitude behavior results in circulation cells in the bottom boundary layer similar to those observed in the wind-forced downwelling problem. These results provide the link sought in the second objective.

We mention that additional numerical experiments concerning the basic two-dimensional spindown problem of a depth-independent coastal jet in a stratified ocean over continental shelf topography show the development of symmetric instabilities and slant-wise convection cells in the bottom boundary layer when the transient Ekman transport is downslope. Results of these experiments will be reported shortly. In addition, studies are in progress on the nature of bottom-layer symmetric instabilities in the three-dimensional wind-forced downwelling circulation, where disturbances that include variations in the alongshore direction are allowed.

Acknowledgments. This research was supported by the Office of Naval Research Coastal Dynamics Program under Grant N00014-93-1-1301 and by the National Science Foundation under Grant OCE-9314317. The authors are grateful to C. Garrett and S. Lentz for thoughtful comments and suggestions. The authors also thank D. Chapman and K. Brink for helpful comments and F. Beyer for typing the manuscript.

APPENDIX A

Other Basic-State Flows

In MacCready and Rhines (1993), the solution for the time-dependent adjustment of the ''arrested Ekman layer'' flow by transient downslope Ekman transport shows the development at early times of a relatively large stable gradient of density at the top of the bottom mixed layer. This is accompanied by an overshoot in magnitude of the alongslope velocity v near the top of the bottom boundary layer compared to the interior v. Similar behavior of the density in the bottom layer was found in transient adjustment problems by Weatherly and Martin (1978) and by Trowbridge and Lentz (1991). Consequently, it is reasonable to question how that type of density structure would affect the linear stability results found in section 3.

A basic-state inviscid, geostrophically balanced, steady flow with a large stable density gradient at the top of the bottom boundary layer can be treated within the present formulation by an appropriate choice of $R(\zeta)$ (2.28). For example, a rapid variation in density and alongshore velocity V at the top of the bottom layer is given by $R = R_{\rm BL}(\zeta)$, where

$$R_{{\rm BL}\zeta} = -1 + \alpha\zeta + (1-\alpha) \times \frac{\left[\exp\left(-\frac{(1-\zeta)}{\epsilon}\right) - \exp\left(-\frac{1}{\epsilon}\right)\right]}{\left[1 - \exp\left(-\frac{1}{\epsilon}\right)\right]}, \quad 0 \le \zeta \le 1, \tag{A.1a}$$

$$R_{{\rm BL}\zeta\zeta} = \alpha + \frac{(1-\alpha)}{\epsilon} \frac{\exp\left[-\frac{(1-\zeta)}{\epsilon}\right]}{\left[1 - \exp\left(-\frac{1}{\epsilon}\right)\right]}, \quad 0 \le \zeta \le 1 \tag{A.1b}$$

and

$$R_{\rm BL}(\zeta) = 0, \qquad \zeta \ge 1, \tag{A.1c}$$

with $\alpha \ge 1$ and $\epsilon \ll 1$. Note that

$$R_{{\rm BL}\zeta}(0) = -1, \qquad R_{{\rm BL}\zeta}(1) = 0, \tag{A.2a,b}$$

so that $R_{{\rm BL}\zeta}$ is continuous at $\zeta = 1$. The resulting variations with ζ of V and $\overline{\rho}$ are shown in Fig. A1 for $\alpha = 1.25$, $\gamma = 1/R_{{\rm BL}\zeta\zeta}(0)$, and for $\epsilon = 0.025$, 0.05, and 0.1, where here

$$V = V_0(1 + R_{{\rm BL}\zeta}), \tag{A.3a}$$

$$\overline{\rho}/\rho_0 = -C_0(\zeta + \xi - \gamma - \gamma R_{{\rm BL}\zeta}), \tag{A.3b}$$

$$C_0 = N_0^2 \delta \cos\alpha/g, \tag{A.3c}$$

and where we plot $V(\zeta)/V_0$ and $\overline{\rho}(\zeta, \xi = 0)/(\rho_0 C_0)$.

Alternatively, we can consider the $\epsilon \to 0$ limit of (A.1), where $R_{\rm BL} \to R_J$, such that

$$R_{J\zeta}(\zeta) = -1 + \alpha\zeta, \quad R_{J\zeta\zeta}(\zeta) = \alpha, \quad 0 \le \zeta < 1, \tag{A.4a,b}$$

and

$$R_J(\zeta) = 0, \qquad \zeta > 1. \tag{A.4c}$$

Note that

$$R_{J\zeta}(0) = -1, \qquad R_{J\zeta}(1) = -1 + \alpha \tag{A.5a,b}$$

so that, for $\alpha > 1$, $R_{J\zeta}$ is discontinuous at $\zeta = 1$. For $\alpha = 1$, $R_J = R_L$ (2.39). We note that the case $N^2 = 0$ for $0 \le \zeta < 1$, corresponding to the arrested Ekman layer solution with R_L, is obtained for $\gamma = \alpha^{-1}$. The resulting ζ variations of V and $\overline{\rho}$, with $R_{J\zeta}$ replacing $R_{{\rm BL}\zeta}$ in (A.3a,b), are also plotted in Fig. A1 for $\alpha = 1.25$ and $\gamma = \alpha^{-1}$.

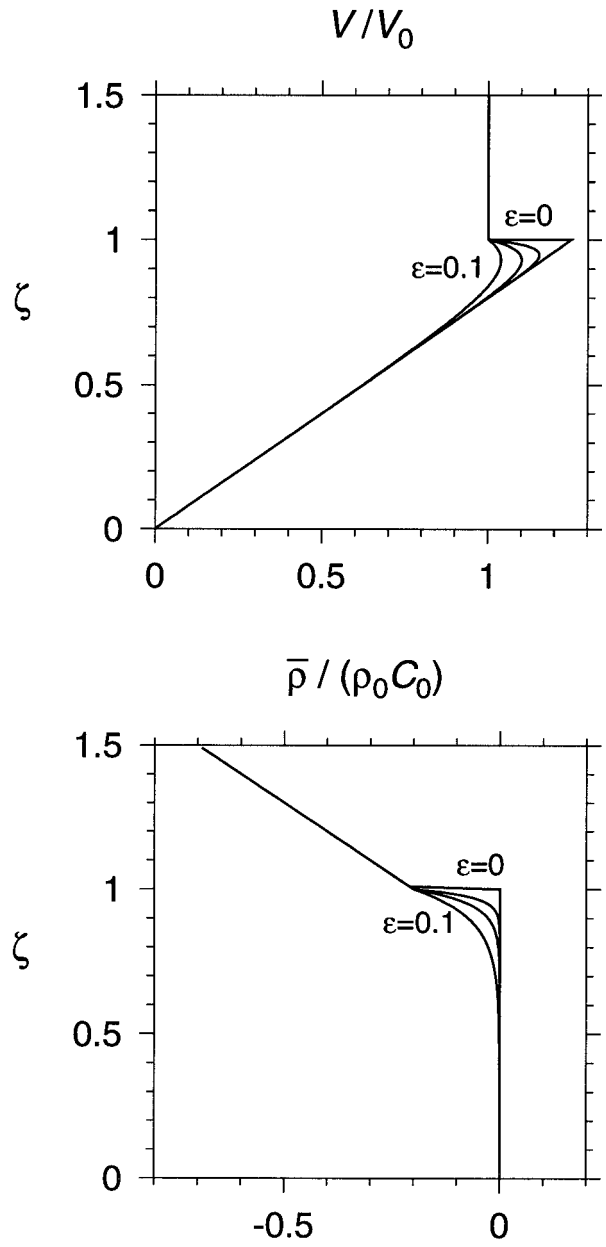

FIG. A1. Variations with ζ of $V(\zeta)/V_0$ and $\overline{\rho}(\zeta, \xi = 0)/(\rho_0 C_0)$ from (A.3a,b) with $\alpha = 1.25$, $\gamma = 1/R_{\mathrm{BL}\zeta\xi}(0)$ for $\epsilon = 0.025$, 0.05, and 0.1. Also shown is the case (denoted by $\epsilon = 0$) with $R_{J\zeta}$ replacing $R_{\mathrm{BL}\zeta}$ in (A.3a,b) and $\alpha = 1.25$, $\gamma = \alpha^{-1}$.

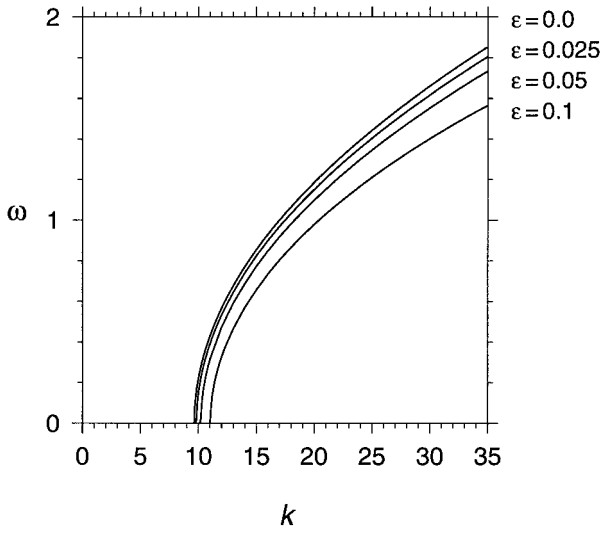

FIG. A2. Growth rates ω of the most unstable mode as a function of wavenumber k obtained from (A.10) with $R = R_J$ (A.4) for $S_0 = 0.4225$, $\alpha = 1.25$, $\gamma = \alpha^{-1}$, and $\gamma_J = 1$ (denoted by $\epsilon = 0$). Also shown are growth rates for the most unstable mode calculated from finite difference solutions to (3.2) and (3.4) with $R_{\zeta\xi} = R_{\mathrm{BL}\zeta\xi}$ (A.1b) for $S_0 = 0.4225$, $\alpha = 1.25$, $\gamma = 1/R_{\mathrm{BL}\zeta\xi}(0)$, and for $\epsilon = 0.025$, 0.05, and 0.1.

With $R = R_J$, the matching conditions for g (3.8) at $\zeta = 1$ need to be reconsidered. Continuity in normal mass flux still requires continuity of g as in (3.17). Integration of (3.8) across a small interval around $\zeta = 1$, from $1 - \Delta\zeta$ to $1 + \Delta\zeta$, followed by the limit $\Delta\zeta \to 0$, gives

$$g_{+\zeta}(1) - g_{-\zeta}(1) = -k^2 S_0 \lambda\gamma g_+(1)[R_{+\zeta}(1) - R_{-\zeta}(1)], \tag{A.6}$$

where $R_{+\zeta}(1) = \lim_{\zeta\downarrow 1} R_\zeta(\zeta)$ and $R_{-\zeta}(1) = \lim_{\zeta\uparrow 1} R_\zeta(\zeta)$. Thus, with $R = R_L$ (2.39) or $R = R_{\mathrm{BL}}$ (A.1), for which $R_{+\zeta}(1) = R_{-\zeta}(1)$, condition (A.6) implies that g_ζ is continuous at $\zeta = 1$ and (A.6) reduces to (3.18).

For $R = R_J$ (A.4), the solution for g is given by (3.15) with γ replaced by γ_J in β_-, where

$$\gamma_J = \alpha\gamma, \tag{A.7}$$

and the condition (A.6) reduces to

$$g_{+\zeta}(1) = g_{-\zeta}(1) + k^2 S_0 \lambda\gamma(\alpha - 1) g_+(1). \tag{A.8}$$

Substituting (3.15a,b) (with γ replaced by γ_J) in (A.8), we obtain

$$\left(1 + \frac{kS_0^{1/2}\gamma(\alpha - 1)}{(1 + \omega^2)^{1/2}}\right) \tan\beta_- = -\frac{\beta_-}{\beta_+}. \tag{A.9}$$

To find $\omega^2(k)$, we write (A.9) in the form

$$k = \frac{(1 + S_0 + \omega^2)\tan^{-1}\theta_J}{S_0^{1/2}[-(1 + \omega^2)(1 - \gamma_J) + \gamma_J S_0]^{1/2}}, \tag{A.10a}$$

$$\theta_J = -\frac{[-(1 + \omega^2)(1 - \gamma_J) - \gamma_J S_0]^{1/2}}{[(1 + \omega^2)^{1/2} + kS_0^{1/2}\gamma(\alpha - 1)]}, \tag{A.10b}$$

and calculate $k = k(\omega^2)$ from (A.10) by iteration, replacing k in θ_J with the previous value calculated from (A.10a).

It is evident from (A.10) that the character of the instability with R_J is qualitatively similar to that found with R_L in section 3. That result is illustrated by the growth rates $\omega = \omega(k)$ for the most unstable mode obtained from (A.10) and plotted in Fig. A2 for $\alpha = 1.25$, $\gamma = \alpha^{-1}$, $\gamma_J = 1$, and $S_0 = 0.4225$. For comparison,

we also include the growth rate for the most unstable mode calculated from finite difference solutions to (3.2) and (3.4) with $R_{\zeta\zeta} = R_{\mathrm{BL}\zeta\zeta}$ (A.1), $\alpha = 1.25$, $\gamma = 1/R_{\mathrm{BL}\zeta\zeta}(0)$, and $S_0 = 0.4225$ for $\epsilon = 0.025$, 0.05, and 0.1. The growth rates curves found with R_{BL} approach that found with R_J for $\epsilon \ll 1$. The growth rates for both R_{BL} and R_J are qualitatively similar to the growth rates found in section 3 for $R = R_L$ and $\gamma = 1$ (Fig. 1). The flow with R_J is a bit more stable as indicated by the increase in value of k_C from 8.6 with $R = R_L$ to 9.6 with $R = R_J$.

APPENDIX B

Effects of Diffusion on Linear Stability

Effects of weak vertical turbulent momentum and density diffusion are included here in the linear stability analysis. The objectives are to find the manner in which weak diffusive processes determine a finite length scale for the onset of instability and also a length scale for maximum growth rate in an unstable basic flow. The approach generally follows that of Walton (1975). For related linear stability results see also Emanuel (1979) and Weber (1980).

We assume constant eddy coefficients and a Prandtl number $\sigma = 1$. The assumption of $\sigma = 1$ results in a somewhat special case for symmetric instabilities (McIntyre 1970; Walton 1975), but it simplifies the analysis, retains the important physical effects, and illustrates the relevant points. The basic-state flow (2.24a,b) is assumed to be unaltered by the effects of diffusion. The governing linearized equations are (2.11) with the addition of vertical diffusion terms. This may be simply accomplished in (2.11) by modifying all of the time derivatives so that

$$\frac{\partial}{\partial t} \rightarrow \frac{\partial}{\partial t} - K_M \frac{\partial^2}{\partial z^2}. \tag{B.1}$$

The governing equation for ψ is then (2.16) with the same modification (B.1). After transformation of coordinates (2.18), nondimensionalization of the independent variables (2.19), neglect of small terms $O(\tan^2\alpha)$, and use of (2.24) for V and N^2, we obtain the following governing equation for ψ corresponding to (2.34):

$$\left(\frac{\partial}{\partial \hat{t}} - \hat{E}\frac{\partial^2}{\partial \zeta^2}\right)^2 \psi_{\zeta\zeta} = -(1 + S_0)\psi_{\zeta\zeta} + 2S_0\psi_{\zeta\xi} - S_0(1 - \gamma R_{\zeta\zeta})\psi_{\xi\xi}, \tag{B.2}$$

where

$$\hat{E} = \delta_E^2/\delta^2, \qquad \delta_E^2 = (K_M/f)\cos^2\alpha. \tag{B.3a,b}$$

We will assume that the dissipative effects are weak, that is,

$$\hat{E} \ll 1. \tag{B.4}$$

Substituting (3.1) in (B.2), we obtain an equation for ϕ corresponding to (3.2):

$$(1 + S_0 + \omega^2)\phi_{\zeta\zeta} - 2ikS_0\phi_\zeta - k^2S_0(1 - \gamma R_{\zeta\zeta})\phi = 2\hat{E}\omega\frac{d^4\phi}{d\zeta^4} - \hat{E}^2\frac{d^6\phi}{d\zeta^6}. \tag{B.5}$$

Boundary conditions for (B.5) consistent with the no-slip conditions and Ekman layer dynamics are

$$\phi = \phi_\zeta = \phi_{\zeta\zeta\zeta} = 0 \quad \text{at } \zeta = 0,\ \zeta_0. \tag{B.6}$$

If we multiply (B.5) by the complex conjugate ϕ^*, subtract the result of multiplying the conjugate of (B.5) by ϕ, and integrate in ζ over the domain using the boundary conditions (B.6), we obtain

$$\omega_i\hat{E}\int_0^{\zeta_0}\phi_{\zeta\zeta}\phi^*_{\zeta\zeta}\,d\zeta + 2\omega_i\omega_r\int_0^{\zeta_0}\phi_\zeta\phi^*_\zeta\,d\zeta = 0, \tag{B.7}$$

where ω_r and ω_i are the real and imaginary parts of $\omega = \omega_r + i\omega_i$. It follows from (B.7) that

$$\omega_i = 0 \quad \text{for } \omega_r \geq 0; \tag{B.8}$$

that is, ω is real for all unstable or marginally stable solutions. This is one simplifying feature of the $\sigma = 1$ case (McIntyre 1970; Walton 1975).

It is convenient to utilize the decomposition (3.7),

$$\phi(\zeta) = \exp(ikS_0\lambda\zeta)g(\zeta) = \exp(ik\hat{\lambda}\zeta)g(\zeta), \tag{B.9}$$

$$\lambda = (1 + S_0 + \omega^2)^{-1} = S_0^{-1}\hat{\lambda}, \tag{B.10}$$

and to solve for g. For $\hat{E} \ll 1$ and large k, the effects of diffusion become important first in the interior rather than through Ekman layers on the boundaries (Walton 1975). This is a result of the $\exp(ikS_0\lambda\zeta)$ dependence of ϕ (B.9). For $E^2 \ll 1$ and

$$k^2 \gg 1, \tag{B.11}$$

the lowest-order effects of diffusion may be determined by utilizing the approximations

$$\frac{d^4\phi}{d\zeta^4} \simeq \hat{\lambda}^4k^4\phi, \qquad \frac{d^6\phi}{d\zeta^6} \simeq -\hat{\lambda}^6k^6\phi, \tag{B.12a,b}$$

in (B.5). The approximations (B.12a,b) are based on (B.11) and the result from section 3 that for the most unstable modes the ζ derivatives of g are $O(1)$. With (B.12a,b), the boundary conditions for (B.5) remain the inviscid conditions (3.4a,b).

With $R = R_L$ so that (3.14) holds, the resulting approximate equations for $g_\pm$ are

$$g_{+\zeta\zeta} - \hat{\beta}_+^2 g_+ = 0, \qquad 1 < \zeta, \tag{B.13a}$$

$$g_{-\zeta\zeta} + \hat{\beta}_-^2 g_- = 0, \qquad 0 \leq \zeta \leq 1, \tag{B.13b}$$

where

$$\hat{\beta}_+^2 = \lambda^2[k^2S_0(1 + \omega^2) + \lambda^{-1}(2\hat{E}\omega\hat{\lambda}^4k^4 + \hat{E}^2\hat{\lambda}^6k^6)], \tag{B.13c}$$

$$\hat{\beta}_-^2 = \lambda^2[k^2S_0[-(1 + \omega^2)(1 - \gamma) + \gamma S_0] - \lambda^{-1}(2\hat{E}\omega\hat{\lambda}^4k^4 + \hat{E}^2\hat{\lambda}^6k^6)], \tag{B.13d}$$

and where we assume $\omega^2 \geq 0$ and $\zeta_0 \to \infty$. The boundary and matching conditions for $g_\pm$ are the same as in section 3, (3.16a,b), (3.17), and (3.18).

The solutions are

$$g_+ = \hat{C}_0 \exp[-\hat{\beta}_+(\zeta - 1)], \qquad 1 < \zeta, \tag{B.14a}$$

$$g_- = \hat{C}_0 \sin(\hat{\beta}_-\zeta)/\sin(\hat{\beta}_-), \qquad 0 \leq \zeta \leq 1, \tag{B.14b}$$

which satisfy (3.16a,b) and (3.17). Application of (3.18) gives the relation

$$\tan\hat{\beta}_- = -\hat{\beta}_-/\hat{\beta}_+, \tag{B.15}$$

which determines $\omega^2 = \omega^2(k, S_0, \gamma, \hat{E})$.

It is necessary that $\hat{\beta}_-^2 \geq 0$ for solutions of (B.15) to exist. The most unstable mode will have

$$\hat{\beta}_-^2 = a_1^2\pi^2, \tag{B.16}$$

as in (3.22), where $\frac{1}{2} < a_1 < 1$. The exact value of a_1 can be obtained from the solution of (B.15), but determination of an exact value for a_1 is not necessary for the following arguments.

We first consider the situation of marginal stability, $\omega = 0$, and, using (B.13d), solve (B.16) for γ:

$$\gamma = (1 + S_0)^{-1} + k^{-2}S_0^{-1} \times [(1 + S_0)a_1^2\pi^2 + \hat{E}^2S_0^6(1 + S_0)^{-6}k^6]. \tag{B.17}$$

In this case, the minimum value of $\gamma(k)$ occurs for

$$k = k_I = \hat{E}^{-1/3}2^{-1/6}(a_1\pi)^{1/3}(1 + S_0)^{7/6}S_0^{-1} \tag{B.18}$$

and is

$$\gamma = \gamma_{CD} = (1 + S_0)^{-1}[1 + 3\hat{E}^{2/3}(a_1^2\pi^2/2)^{2/3}S_0(1 + S_0)^{-1/3}]. \tag{B.19}$$

Thus, inclusion of diffusive effects results in the existence of a critical wavenumber k_I (B.18) for the onset of instability and also in stabilization of the flow since $\gamma_{\rm CD} > \gamma_C = (1 + S_0)^{-1}$ (3.24). The wavenumber k_I scales as $\hat{E}^{-1/3}$ while $\lambda_{\rm CD} - \lambda_C = O(\hat{E}^{2/3})$, similar to the results of Walton (1975).

The dimensional wavelength corresponding to k_I, with $\gamma = \gamma_{\rm CD} \simeq (1 + S_0)^{-1}$, is

$$\lambda_I^{(x')} = 2\pi\delta(k_I \tan\alpha)^{-1} \tag{B.20a}$$

$$\simeq \frac{V_0\hat{E}^{1/3}}{f}\left[\frac{2\pi 2^{1/6}\cos\alpha}{(a_1\pi)^{1/3}(1 + S_0)^{1/6}}\right], \tag{B.20b}$$

which shows that $\lambda_I^{(x')}$ scales as V_0/f. The importance of the scaling dependence of $\lambda_I^{(x')}$ on V_0/f was emphasized by Emanuel (1979), who argued, with reference to Walton's (1975) results, that the dependence of $\lambda_I^{(x')}$ on $\hat{E}$ through the function $\hat{E}^{1/3}$ was fairly weak; that is, $\hat{E}^{1/3}$ was near $O(1)$, unless $\hat{E}$ was extremely small. A similar argument may be made here for a weak dependence of $\lambda_I^{(x')}$ on S_0, since that is through the function $(1 + S_0)^{-1/6}$.

Next we consider an unstable flow with $\gamma_{\rm CD} < \gamma < 1$ and $\omega > 0$. From (B.16) we obtain

$$\omega^2 = (1 - \gamma)^{-1}\{\gamma S_0 - (1 - \gamma) - k^{-2}S_0^{-1}(1 + S_0 + \omega^2) \times [a_1^2\pi^2(1 + S_0 + \omega^2) + (2\hat{E}\omega\hat{\lambda}^4k^4 + \hat{E}^2\lambda^6k^6)]\}. \tag{B.21}$$

For $k^2 \gg 1$, $\hat{E} \ll 1$, and $\gamma_{\rm CD} \leq \gamma < 1$ we can solve (B.21) for ω^2 iteratively by taking as the first approximation,

$$\omega^2 \simeq \omega_{(0)}^2 = (1 - \gamma)^{-1}[\gamma S_0 - (1 - \gamma)]. \tag{B.22}$$

Utilizing (B.22), we obtain

$$(1 + S_0 + \omega^2) \simeq (1 + S_0 + \omega_{(0)}^2) = S_0(1 - \gamma)^{-1}, \tag{B.23}$$

$$\hat{\lambda} \simeq \hat{\lambda}_{(0)} = S_0(1 + S_0 + \omega_{(0)}^2)^{-1} = (1 - \gamma). \tag{B.24}$$

The next approximation for ω^2 is

$$\omega^2 \simeq \omega_{(0)}^2 - (1 - \gamma)^{-2}k^{-2}[a_1^2\pi^2S_0(1 - \gamma)^{-1} + 2\hat{E}\omega_{(0)}\hat{\lambda}_{(0)}^4k^4 + \hat{E}^2\hat{\lambda}_{(0)}^6k^6]. \tag{B.25}$$

If we consider $\omega_{(0)} = O(1)$, we find

$$2\hat{E}\omega_{(0)}\hat{\lambda}_{(0)}^4k^4 \gg \hat{E}^2\hat{\lambda}_0^6k^6 \quad \text{for } \hat{E}k^4 = O(1), \tag{B.26}$$

which implies that the last term in (B.25) is relatively small and may be neglected. It follows that the maximum of $\omega^2(k)$ occurs for

$$k = k_M \simeq \hat{E}^{-1/4}\left(\frac{a_1^2\pi^2S_0}{2}\right)^{1/4}(1 - \gamma)^{-5/4}\omega_{(0)}^{-1/4} \tag{B.27}$$

and is

$$\omega^2 = \omega_{\rm MD}^2 \simeq \omega_{(0)}^2 - k_M^{-2}(1 - \gamma)^{-3}2a_1^2\pi^2S_0. \tag{B.28}$$

Consequently, for a given unstable flow with $\gamma_{\rm CD} < \gamma < 1$ inclusion of diffusive effects results in the existence of a wavenumber k_M (B.27) for maximum growth rate $\omega_{\rm MD}$, where $\omega_{\rm MD}$ is decreased from the inviscid value $\omega_M = \omega_{(0)}$. The wavenumber k_M scales as $\hat{E}^{-1/4}$, while $\omega_M^2 - \omega_{\rm MD}^2 = O(\hat{E}^{1/2})$. For the basic-state flow with $\gamma \to 1$, however, we find that the leading order behavior for $k \gg 1$ is still given by (3.28) and that the maximum growth rate $\omega \to \infty$ for $k \to \infty$, similar to the inviscid result.

The dimensional wavelength corresponding to k_M is

$$\lambda_M^{(x')} = \frac{V_0\hat{E}^{1/4}}{f}\left[\frac{2\pi 2^{1/4}\cos\alpha(1 - \gamma)^{11/8}}{(a_1\pi)^{1/2}\gamma S_0^{5/4}(\gamma - 1 + \gamma S_0)^{1/8}}\right], \tag{B.29}$$

which, similar to $\lambda_I^{(x')}$ (B.20), shows a scaling dependence on V_0/f and a weak dependence on $\hat{E}$.

REFERENCES

Allen, J. S., and P. A. Newberger, 1996: Downwelling circulation on the Oregon continental shelf. Part I: Response to idealized forcing. *J. Phys. Oceanogr.,* **26,** 2011–2035.

Bennetts, D. A., and B. J. Hoskins, 1979: Conditional symmetric instability—A possible explanation for frontal rain bands. *Quart. J. Roy. Meteor. Soc.,* **105,** 945–962.

Bishop, C. H., and C. Chen, 1995: Symmetric instability and baroclinic boundary layers. Preprints, *Tenth Conf. on Atmospheric and Oceanic Waves and Stability,* Big Sky, MT, Amer. Meteor. Soc., 31–32.

Blumberg, A. F., and G. L. Mellor, 1987: A description of a three-dimensional coastal circulation model. *Three Dimensional Coastal Ocean Models,* N. Heaps, Ed., Coastal and Estuarine Sci. Series, Vol. 4, Amer. Geophys. Union, 1–16.

Chapman, D. C., and S. J. Lentz, 1997: Adjustment of stratified flow over a sloping bottom. *J. Phys. Oceanogr.,* **27,** 340–356.

Emanuel, K. A., 1979: Inertial instability and mesoscale convective systems. Part I: Linear theory of inertial instability in rotating viscous fluids. *J. Atmos. Sci.,* **36,** 2425–2449.

——, 1994: *Atmospheric Convection.* Oxford University Press, 580 pp.

Galperin, B., L. H. Kantha, S. Hassid, and A. Rosati, 1988: A quasi-equilibrium turbulent energy model for geophysical flows. *J. Atmos. Sci.,* **45,** 55–62.

Garrett, C., P. MacCready, and P. Rhines, 1993: Boundary mixing and arrested Ekman layers: Rotating stratified flow near a sloping boundary. *Annu. Rev. Fluid Mech.,* **25,** 291–323.

Holton, J. R., 1992: *An Introduction to Dynamic Meteorology.* 3d ed. Academic Press, 511 pp.

Hoskins, B. J., 1974: The role of potential vorticity in symmetric stability and instability. *Quart. J. Roy. Meteor. Soc.,* **100,** 480–482.

MacCready, P., and P. B. Rhines, 1993: Slippery bottom boundary layers on a slope. *J. Phys. Oceanogr.,* **23,** 5–22.

McIntyre, M. E., 1970: Diffusive destabilization of the baroclinic circular vortex. *Geophys. Fluid Dyn.,* **1,** 19–57.

Mellor, G. L., and T. Yamada, 1982: Development of a turbulence closure model for geophysical fluid problems. *Rev. Geophys. Space Phys.,* **20,** 851–875.

Miller, T., 1984: The structure and energetics of fully nonlinear symmetric baroclinic waves. *J. Fluid Mech.,* **142,** 343–362.

Ooyama, K., 1966: On the stability of the baroclinic circular vortex: A sufficient criterion for instability. *J. Atmos. Sci.,* **23,** 43–53.

Pacanowski, R. C., and S. G. H. Philander, 1981: Parameterization of vertical mixing in numerical models of tropical oceans. *J. Phys. Oceanogr.,* **11,** 1443–1451.

Stone, P. H., 1966: On non-geostrophic baroclinic instability. *J. Atmos. Sci.,* **23,** 390–400.

——, 1970: On non-geostrophic baroclinic instability. Part II. *J. Atmos. Sci.,* **27,** 721–726.

Thorpe, A. J., and R. Rotunno, 1989: Nonlinear aspects of symmetric instability. *J. Atmos. Sci.,* **46,** 1285–1299.

Trowbridge, J. H., and S. J. Lentz, 1991: Asymmetric behavior of an oceanic boundary layer over a sloping bottom. *J. Phys. Oceanogr.,* **21,** 1171–1185.

Walton, I. C., 1975: The viscous nonlinear symmetric baroclinic instability of a zonal shear flow. *J. Fluid Mech.,* **68,** 757–768.

Weatherly, G. L., and P. J. Martin, 1978: On the structure and dynamics of the ocean bottom boundary layer. *J. Phys. Oceanogr.,* **8,** 557–570.

Weber, J. E., 1980: Symmetric instability of stratified geostrophic flow. *Tellus,* **32,** 176–185.

Winters, K. B., P. N. Lombard, J. J. Riley, and E. A. D'Asaro, 1995: Available potential energy and mixing in density-stratified fluids. *J. Fluid Mech.,* **289,** 115–128.